Autonomous ROV inspections of aquaculture net pens using DVL

Herman B. Amundsen, *Member, IEEE,* Walter Caharija, *Senior Member, IEEE,*
and Kristin Y. Pettersen, *Fellow, IEEE*

***Abstract*—This paper presents a method for guiding a remotely operated vehicle (ROV) to autonomously traverse an aquaculture net pen. The method is based on measurements from a Doppler velocity log (DVL) and uses the measured length of the DVL beam vectors to approximate the geometry of a local region of the net pen in front of the ROV. The ROV position and orientation relative to this net pen approximation are used as inputs to a nonlinear guidance law. The guidance law is based upon the line-of-sight (LOS) guidance law. By utilizing that an ROV is fully-actuated in the horizontal plane, the crosstrack error is minimized independently of the ROV heading. A Lyapunov analysis of the closed-loop system with this guidance law shows that the ROV is able to follow a continuous path in the presence of a constant irrotational ocean current. Finally, results from simulations and experiments demonstrating the performance of the net pen approximation and control system are presented.**

***Index Terms*—Line-of-sight (LOS) guidance, Doppler-velocity-log (DVL), path following, nonlinear control, remotely operated vehicle (ROV), aquaculture**

I. Introduction

THE aquaculture industry is one of the fastest-growing food production industries [1]. As the industry is up-scaling, so are the challenges in maintaining a sustainable and environmentally friendly production. Fish escaping through net holes is a great challenge, and in 2010 it was reported that more than two-thirds of the registered fish escape incidents in the Norwegian aquaculture industry stem from holes in the net [2]. Escapes from fish farms are a threat to the wild fish population, for example from the transfer of diseases or alteration of wild fish genetics through interbreeding. Another big challenge is the biofouling of net pens, as this leads to low oxygen levels which are crucial for fish health and welfare [3]. Inspection, maintenance and repair operations of net pens are important countermeasures against these threats.

Traditionally, divers have been used for inspection operations in net pens. However, diving operations are exposed to risk, which is a key motivation for replacing divers with remotely operated vehicles (ROVs), a development that has been increasing for the last decade. The ROV pilot manually steers the ROV based on information from a forward-looking camera and instruments such as compass and depth sensors. Due to water flow turbidity, lighting conditions and surrounding biomass, piloting of ROVs is challenging, and full coverage of the net cannot be expected. To enable safe and reliable inspections of net pens, new control methods are required. Furthermore, there is an ongoing effort towards developing new methods in aquaculture robotics that can enable remote or autonomous operations [4], which will both increase safety and reduce operational costs. To the authors' knowledge, there are no industrial companies which have successfully managed to implement autonomous inspections of net pens, and this remains a relevant topic of research.

ROVs are versatile vehicles capable of hovering and intervention tasks and are used for a wide variety of different operations, e.g. inspection of subsea structures, underwater mapping and underwater archaeology. As the introduction of ROVs in aquaculture is relatively recent, the design of ROVs has been optimized towards other industries. However, ROV operations in aquaculture face unique challenges, such as operating in the wave-zone, the avoidance of cable entanglement and minimizing the stressing of fish. The challenges in aquaculture robotics operations therefore also highlight a need for specialized designs of underwater vehicles, which have been addressed in several articles [5], [6], [7], [8].

A trend in recent years is to relocate aquaculture sites to locations exposed to harsh environmental loads [9]. This is motivated by greater water flows, which are beneficial in terms of waste dispersal and water quality, as well as the lack of available sheltered locations. Conditions such as current speeds of 0.6 ms^{-1} and significant wave heights of 3.5 m have been reported in these new aquaculture locations [10]. As aquaculture net pens are flexible structures, they are deformed by current-induced drag forces [11]. For current velocities over 0.6 ms^{-1}, a reduced net pen volume of 30 % has been reported [12]. Due to this flexible nature, it is extremely difficult to predetermine the shape and the position of the net pens. Navigation for net pen operations therefore has to be done relative to an unknown and dynamic net pen shape.

In [13], [14] a method for autonomous underwater vehicle (AUV) navigation along aquaculture net pens using computer vision techniques is suggested. The AUV is navigated towards an object fixed to the net pen with known heading and depth. The object is detected from camera images and the AUV is commanded to follow a predetermined route relative to the object. Although this method presents a novel approach, it also has some clear limitations. Firstly, the method is dependent on a target object with known heading and depth. Secondly, the desired path relative to the detected objects is generated

H. B. Amundsen is with SINTEF Ocean AS and the Department of Engineering Cybernetics, Norwegian University of Science and Technology, both located in Trondheim, Norway. herman.biorn.amundsen@sintef.no

W. Caharija is with SINTEF Ocean AS, Trondheim, Norway. walter.caharija@sintef.no

K. Y. Pettersen is with the Center for Autonomous Operations and Systems, Norwegian University of Science and Technology, Trondheim, Norway. kristin.y.pettersen@ntnu.no

offline and is therefore not robust to potential deformations in net pens.

In [15], a method for approximating the seafloor geometry by the use of a Doppler velocity log (DVL) directed towards the seabed is proposed. Based on the DVL measured altitude, the seafloor is, at each time step, approximated as a plane. Furthermore, an ROV altitude control law is proposed, where the ROV altitude and seafloor gradient are used as inputs. The control law extends the work of [16], which proposes a bottom-following ROV control law based upon measurements from two echo-sounders. In [17], an experimental evaluation of the performance of DVLs in net pens is conducted. Here it is shown that a DVL successfully interacts with a net pen, which suggests that DVLs may be used for navigational purposes in net pens.

The first contribution of this paper is a modification of the method in [15], where the geometry of a local region of the net pen is approximated by using a DVL aimed towards the net surface in front of the ROV. This allows ROV navigation along a dynamic net pen shape, and the ROV position and orientation relative to the approximated net pen can then be used as inputs by the motion control system.

To perform autonomous inspection, we will solve the corresponding path following problem. Path following is the challenge of guiding a vehicle to follow a desired path. Line-of-sight (LOS) guidance is a nonlinear guidance law which successfully has been implemented on marine vehicles to achieve path following, see for instance [18] and [19]. It ranks among the most popular path following algorithms due to its simplicity and intuitiveness. The method mimics a helmsman steering the vehicle towards a point lying at a constant distance ahead of the vehicle along the desired path [20]. Typically, the input to the guidance law is the desired path or desired waypoints, and its output is a desired heading angle which will minimize the distance to the path when the vehicle is moving at a positive speed. In [21], it is shown that LOS guidance will achieve uniform semi-global exponential stability (USGES) for path following of continuous paths, while [22] extends the result to include an unknown ocean current.

A drawback of LOS guidance is that it is susceptible to environmental disturbances, such as waves and currents, if the crab angle cannot be measured. In [20], it is suggested adding integral action to the LOS guidance law to counter constant or slowly-varying disturbances. For straight-line path following in the presence of constant and slowly-varying disturbances, [23] shows that integral line-of-sight (ILOS) guidance law will achieve uniform global asymptotical stability (UGAS) and uniform local exponential stability (ULES). The ILOS guidance law introduces a non-zero steady-state crab angle to counter constant disturbances. In [24], it is shown how saturated transverse actuators can reduce the crab angle the vehicle has to hold.

LOS guidance was first developed as a solution to the underactuated path following control problem. Most marine surface vessels are underactuated, as they are only equipped with fixed stern propellers and rudders. This is also the case when azimuth thrusters or transverse tunnel-thrusters are installed, as the aft propellers will be dominant during transit. ROVs, on the other hand, commonly have the thrusters arranged such that they are actuated in surge, sway, heave and yaw. They can therefore be considered fully-actuated in the horizontal plane. The principles for LOS guidance is as applicable for fully-actuated vehicles as for underactuated vehicles. However, for fully-actuated vehicles, the LOS algorithm will output the desired velocity vector needed for path following as mentioned in [25] and [26]. By controlling the surge and sway velocity, the ROV heading angle is decoupled from the desired course angle, and path following is achieved independently of the heading. The course angle can thus be controlled using a LOS algorithm, while the heading angle can then be controlled to follow some auxiliary objective. For inspection tasks, this can be advantageous, as the camera-view, which is aligned with the ROV heading, can be directed towards the objects of interest instead of being dictated by the path.

The second contribution of this paper is the development of a new LOS guidance law for vehicles fully-actuated in the horizontal plane. A set of adaptive feedback linearizing control laws is suggested, and using cascaded system theory it is shown that the crosstrack error converges asymptotically to zero independently of the heading. The results are valid for continuously curved paths in the presence of constant and irrotational ocean currents.

The paper is organized as follows. Section II presents the vehicle model for control design purposes. Section III describes the DVL velocity measurements and beam vectors. Section IV presents an overview of the proposed method. In Section V we propose a method for approximating the geometry of a local region of the net pen based on the DVL measurements. In Section VI we propose the guidance and control laws which will satisfy the path-following problem. Section VII shows that the closed-loop system with the guidance law and control laws can be analyzed as a cascade and presents the stability analysis. Finally, Section VIII presents results from simulations and full-scale sea trials.

II. Vehicle Model

The ROV is described in 3 DOF; surge, sway, and yaw. The kinematics of the vehicle are given in the North-East-Down (NED) frame, denoted $\{n\}$, while the dynamics are described in the body-fixed coordinate frame, denoted $\{b\}$.

Assumption 1. The ROV is symmetric in port-starboard, fore-aft and bottom-top.

Assumption 2. The roll and pitch motion is passively stabilized by gravity, and can therefore be neglected.

Assumption 3. The vehicle is neutrally buoyant, and the motion in heave can therefore be neglected. Furthermore, the vehicle center of gravity (CG) and the center of buoyancy (CB) are located along the same vertical axis in $\{b\}$.

Remark 1. Most ROVs are designed to be slightly positively buoyant. This means that they are for all practical purposes neutrally buoyant, but in the case of a system shut down the ROV will slowly rise to the surface.

Assumption 4. The body-fixed frame center of origin (CO) is located in the CG.

Remark 2. Assumptions 1-4 are common assumptions in ROV modeling, see for instance [27, Ch. 2] and [28].

The state of the ROV is given by the vector $[\boldsymbol{\eta}^T, \boldsymbol{\nu}^T]^T$. Here, $\boldsymbol{\eta} = [x, y, \psi]^T$ is a generalized vector describing the position and orientation of the ROV in $\{n\}$, while $\boldsymbol{\nu} = [u, v, r]^T$ describes the linear and angular velocity of the ROV in $\{b\}$. The vehicle is under the influence of an ocean current.

Assumption 5. The current is constant, irrotational and bounded with velocity vector $\boldsymbol{V}_c = [V_x, V_y, 0]^T$ in $\{n\}$. Hence, there exists a constant $V_{\max} > 0$ such that $V_{\max} > \sqrt{V_x^2 + V_y^2}$. Furthermore, the time-derivative is $\dot{\boldsymbol{V}}_c = \boldsymbol{0}$.

The maneuvering model [29, Ch. 7] of the ROV is considered:

$$\dot{\boldsymbol{\eta}} = \boldsymbol{R}(\psi)\boldsymbol{\nu} \tag{1}$$

$$\boldsymbol{M}_{RB}\dot{\boldsymbol{\nu}} + \boldsymbol{C}_{RB}(\boldsymbol{\nu})\boldsymbol{\nu} + \boldsymbol{M}_A\dot{\boldsymbol{\nu}}_r + \boldsymbol{C}_A(\boldsymbol{\nu}_r)\boldsymbol{\nu}_r + \boldsymbol{D}\boldsymbol{\nu}_r = \boldsymbol{B}\boldsymbol{f} \tag{2}$$

The matrix $\boldsymbol{R}(\psi)$ is the principal rotation matrix around the z-axis. Moreover, $\boldsymbol{\nu}_r \triangleq \boldsymbol{\nu} - \boldsymbol{\nu}_c$ is the relative velocity between the vehicle and the ocean current, where $\boldsymbol{\nu}_c = \boldsymbol{R}^T(\psi)\boldsymbol{V}_c = [u_c, v_c, 0]^T$ is the current velocity expressed in $\{b\}$.

The matrix $\boldsymbol{M}_{RB} = \boldsymbol{M}_{RB}^T > 0$ is the rigid-body inertia matrix, $\boldsymbol{M}_A = \boldsymbol{M}_A^T > 0$ is the hydrodynamic added mass inertia matrix, $\boldsymbol{C}_{RB}$ is the rigid-body centripetal and Coriolis matrix, $\boldsymbol{C}_A$ is the added mass centripetal and Coriolis matrix, and $\boldsymbol{D} > 0$ is the damping matrix.

For control purposes, the matrices $\boldsymbol{R}(\psi), \boldsymbol{M}_{RB}, \boldsymbol{M}_A$ and $\boldsymbol{D}$ can be considered having the following structure:

$$\boldsymbol{R}(\psi) \triangleq \begin{bmatrix} \cos(\psi) & -\sin(\psi) & 0 \\ \sin(\psi) & \cos(\psi) & 0 \\ 0 & 0 & 1 \end{bmatrix}, \ \boldsymbol{M}_i \triangleq \begin{bmatrix} m_{11}^i & 0 & 0 \\ 0 & m_{22}^i & 0 \\ 0 & 0 & m_{33}^i \end{bmatrix} \tag{3}$$

$$\boldsymbol{D} \triangleq \begin{bmatrix} d_{11} & 0 & 0 \\ 0 & d_{22} & 0 \\ 0 & 0 & d_{33} \end{bmatrix} \tag{4}$$

where $i \in \{RB, A\}$.

Assumption 6. The damping is linear.

Remark 3. Nonlinear damping is not considered in order to reduce the complexity of the controllers. For low-speed maneuvering, which is common for aquaculture ROV operations, Assumption 6 is a mild assumption as linear damping will dominate its nonlinear counterpart. Furthermore, any nonlinear damping should enhance the directional stability of the vehicle due to the passive nature of the hydrodynamic damping forces. In general, unmodeled dynamics such as nonlinear damping may affect the tracking performance of the control system and should be addressed by robust control techniques such as adaptive control or integral action.

The matrix $\boldsymbol{B} \in \mathbb{R}^{3xn}$ is a constant thrust allocation matrix which maps the control input vector $\boldsymbol{f} \in \mathbb{R}^n$ to the forces and moments acting on the vehicle, where $n \geq 3$ is the number of thrusters working in surge, sway and yaw. The control forces and moments acting on the vehicle are described by the vector $[\tau_u, \tau_v, \tau_r]^T \triangleq \boldsymbol{M}^{-1}\boldsymbol{B}\boldsymbol{f}$, where $\boldsymbol{M} \triangleq \boldsymbol{M}_{RB} + \boldsymbol{M}_A$. The centripetal and Coriolis matrix $\boldsymbol{C}$ is obtained from $\boldsymbol{M}_i$ by [29, Ch. 7]:

$$\boldsymbol{C}_i(\boldsymbol{\nu}) \triangleq \begin{bmatrix} 0 & 0 & -m_{22}^i v \\ 0 & 0 & m_{11}^i u \\ m_{22}^i v & -m_{11}^i u & 0 \end{bmatrix} \tag{5}$$

where $i \in \{RB, A\}$.

Assumption 7. The thrust allocation matrix $\boldsymbol{B}$ has full rank, i.e. $\mathrm{rank}(\boldsymbol{B}) = 3$, so that the ROV is fully actuated in surge, sway and yaw.

Remark 4. The size and elements of the matrix $\boldsymbol{B}$ are dependent on the thruster configuration, and for the generality of the theoretical results will not be further specified here beyond the requirement in Assumption 7. The model of the ROV used in simulations and experiments will be given in Section VIII.

A. Component Form

In order to solve the nonlinear control design problem, it can useful to expand (1) and (2) into component form. By using that the time-derivative of the current velocity in $\{b\}$ is

$$\dot{\boldsymbol{\nu}}_c = \frac{d}{dt}(\boldsymbol{R}^T(\psi)\boldsymbol{V}_c) = [rv_c, -ru_c, 0]^T, \tag{6}$$

the 3DOF vehicle model can be written as

$$\dot{x} = \cos(\psi)u - \sin(\psi)v \tag{7a}$$

$$\dot{y} = \sin(\psi)u + \cos(\psi)v \tag{7b}$$

$$\dot{\psi} = r \tag{7c}$$

$$\dot{u} = -\frac{d_{11}}{m_{11}}u + \frac{m_{22}}{m_{11}}vr + \boldsymbol{\phi}_u^T(\psi, r)\boldsymbol{\theta}_u + \tau_u \tag{7d}$$

$$\dot{v} = -\frac{d_{22}}{m_{22}}v - \frac{m_{11}}{m_{22}}ur + \boldsymbol{\phi}_v^T(\psi, r)\boldsymbol{\theta}_v + \tau_v \tag{7e}$$

$$\dot{r} = -\frac{d_{33}}{m_{33}}r + \frac{m_{11} - m_{22}}{m_{33}}uv + \boldsymbol{\phi}_r^T(u, v, \psi)\boldsymbol{\theta}_r + \tau_r \tag{7f}$$

where $m_{ij} \triangleq m_{ij}^{RB} + m_{ij}^A$, $\boldsymbol{\theta}_u = \boldsymbol{\theta}_v = [V_x, V_y]^T$ and $\boldsymbol{\theta}_r = [V_x, V_y, V_x^2, V_y^2, V_x V_y]^T$. The expressions for $\boldsymbol{\phi}_u(\psi, r), \boldsymbol{\phi}_v(\psi, r)$ and $\boldsymbol{\phi}_r(u, v, \psi)$ are given in Appendix A.

III. DVL Measurements

DVLs are widespread in maritime applications. Typically, they are mounted on a vehicle to measure the velocity of the vehicle with respect to the seabed. They consist of a transducer head which sends multiple hydro-acoustic signals towards the seabed. The velocity is then calculated by measuring the Doppler shift in the reflected acoustic signals. The most common DVL configuration is the Janus configuration, which consists of four transducers pointing towards the fore, aft, port and starboard of the vehicle.

The DVL measurements are described in a DVL-fixed reference frame, denoted $\{d\}$. Furthermore, the position and orientation of the DVL relative to the body-fixed reference

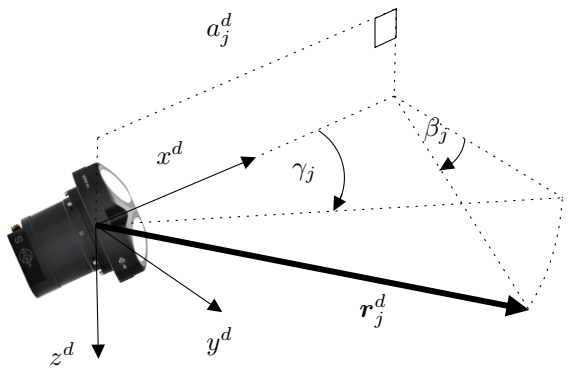

Fig. 1. The DVL jth beam vector components.

frame $\{b\}$ is known and fixed, and is described by the vector $\boldsymbol{r}^b_{b/\text{dvl}} = [x^b_{b/\text{dvl}}, y^b_{b/\text{dvl}}, z^b_{b/\text{dvl}}]^T$ from the CO to the origin of $\{d\}$ expressed in $\{b\}$, and the rotation matrix $\boldsymbol{R}^b_d(\boldsymbol{\Theta}_{db}) \in \mathbb{R}^{3x3}$ from $\{b\}$ to $\{d\}$, where $\boldsymbol{\Theta}_{db} \in \mathbb{R}^3$ is the known rotation in Euler angles.

A. DVL Measured Velocity

The DVL measured velocity in the body-fixed frame is given by [25]

$$\boldsymbol{v}^b_{d/n} = [u, v, 0]^T + [0, 0, r]^T \times \boldsymbol{r}^b_{b/\text{dvl}} + \boldsymbol{R}^b_d(\boldsymbol{\Theta}_{db})\boldsymbol{w}^d_{\text{dvl}} \quad (8)$$

Here, $\boldsymbol{v}^b_{d/n} \in \mathbb{R}^3$ is the measured velocity expressed in $\{b\}$, while $\boldsymbol{w}^d_{\text{dvl}} \in \mathbb{R}^3$ is the measurement noise.

B. DVL Beam Vectors

In this paper, the DVL is mounted on the ROV so that it points towards the front of the ROV with $\boldsymbol{R}^b_d(\boldsymbol{\Theta}_{db}) = \mathbb{I}_3$. The DVL jth beam is shown in Fig. 1, and is represented by the vector

$$\boldsymbol{r}^d_j = \begin{bmatrix} x^d_j \\ y^d_j \\ z^d_j \end{bmatrix} = a^d_j \begin{bmatrix} 1 \\ \tan(\gamma_j)\cos(\beta_j) \\ \tan(\gamma_j)\sin(\beta_j) \end{bmatrix} \quad (9)$$

where a^d_j is the horizontal component of $\boldsymbol{r}^d_j$, γ_j the rotation about the DVL z^d axis and β_j the rotation about the x^d axis. The angles β_j, γ_j are constant and known, while a^d_j is measured.

IV. Method Overview

There exist numerous different designs of net pens. One of the most most common, however, is the circular net cage, which consists of a circular floating collar, a number of vertical net walls and a conic shape bottom, see Fig. 2. The size of the net cages can range between diameters of a few dozen meters to diameters of more than 100m. Due to the flat structure of the net walls, a horizontal projection can roughly be considered as a set of several straight lines connected at the mooring points, and the motion control objective can therefore often be simplified to consecutive straight line path following problems.

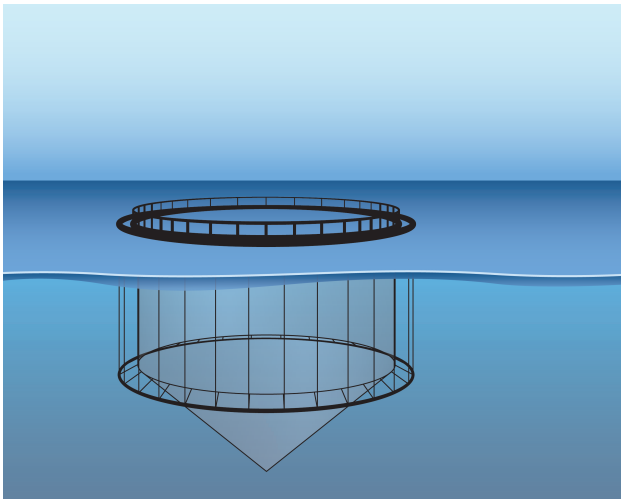

Fig. 2. Circular net cage with sinker tube.

The goal of this paper is to design a control method which directs the ROV heading towards the net pen and makes the ROV traverse the net pen with a desired distance and speed. This way, the camera view is directed towards the net, i.e. the object of interest, while the ROV follows the net pen in a controlled manner. As net pens are flexible structures that will be deformed by currents, predetermined paths calculated offline are unsuited for net pen following. Instead, we will make an online approximation of a local region of the net pen. From this approximation, we will estimate the ROV position and orientation relative to the net pen and develop a motion controller that produces the thruster inputs which make the ROV follow the net pen. We will do this through the following 4 steps:

1) At each time step, based on the DVL measurements, approximate a local region of the net pen in front of the ROV as a linear plane, see Figure 4.
2) Determine the ROV distance and yaw angle relative to the plane approximation.
3) Control the ROV heading, so that the ROV is directly facing the plane approximation.
4) Through LOS guidance and velocity control, traverse the approximated net pen with a desired distance and speed.

Approximating a local region of the net pen as a plane will accurately capture the flat structure of the net walls, but will not capture curves or other unusual shapes that might occur due to mooring or ocean currents. However, as the net pen approximation is updated at each time step, the method should nonetheless quickly compensate for approximation errors.

Figure 3 presents a schematic diagram of the proposed control system. The operator specifies the desired distance to the net, as well as the desired ROV speed. The net pen approximation uses the DVL measurements to compute the reference signals for the guidance law and yaw controller. The guidance law computes the desired surge and sway velocity through LOS guidance. Finally, the surge, sway and yaw controllers compute the control forces vector $\boldsymbol{\tau}$.

Remark 5. This paper focuses on the control and autonomy

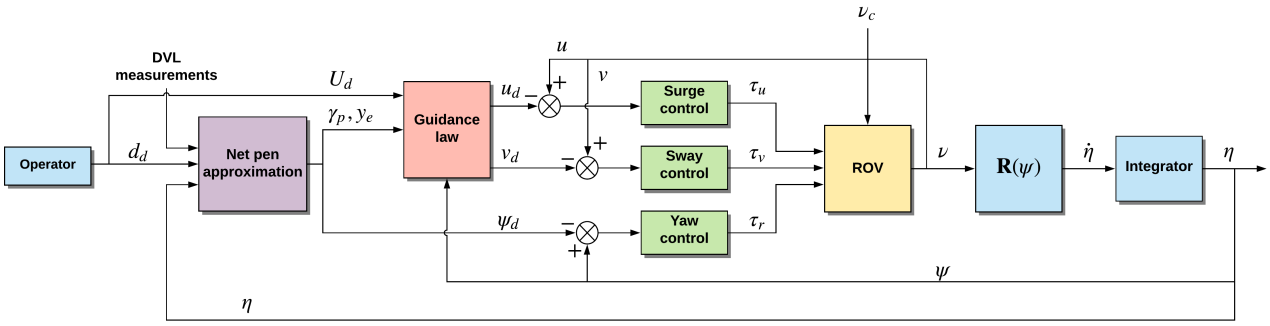

Fig. 3. Control scheme for autonomous net pen following. The operator specifies the desired ROV speed U_d and desired distance d_d relative to the net pen. The net pen approximation uses the measured DVL beam vectors to compute the references for the guidance law and yaw controller, while the guidance law calculates the references for the surge and sway velocity controllers. The surge, sway and yaw controllers compute the control forces and moments $\boldsymbol{\tau} = [\tau_u, \tau_v, \tau_r]^T$.

side of the architecture shown in Figure 3. The operator interaction aspect, although fundamental for successful execution of net pen inspection missions, is out of scope.

V. Net Pen Geometry Approximation by the use of a DVL

This section proposes a method for approximating the geometry of a local region of the net pen in front of the ROV based upon the DVL measurements. It is assumed that the net pen can be approximated as a linear plane given by the equation

$$f(x, y, z) = -x + by + cz + d = 0 \tag{10}$$

expressed in $\{d\}$, where f can be calculated from the four DVL beams. Furthermore, this section shows how one can calculate the ROV yaw angle and distance relative to the approximated net pen.

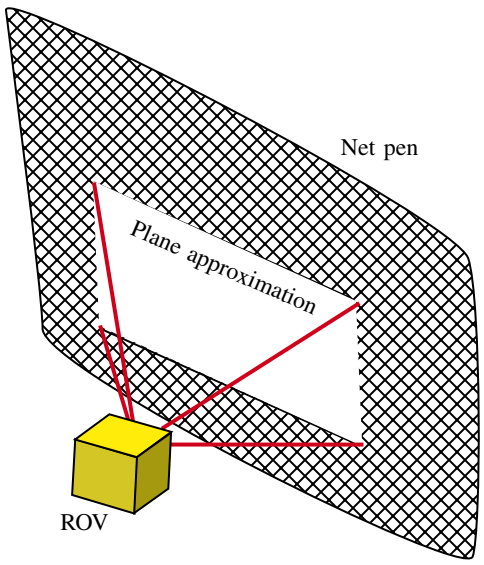

Fig. 4. Approximating a net pen as a linear plane (white) by the use of 4 DVL beams (red).

A. Net Pen Approximation

From a set of three points, it is possible to construct a plane. Therefore, the plane approximation f can be obtained from a set of three returning DVL beams. Furthermore, from a set of four returning DVL beams, the plane approximation can be obtained through a least squares regression. This can be done by minimizing the objective function

$$\sum_{J=1}^{4} [a_j^d - (by_j^d + cz_j^d + d)]^2 \tag{11}$$

The system

$$\boldsymbol{Ax} = \begin{bmatrix} y_1^d & z_1^d & 1 \\ y_2^d & z_2^d & 1 \\ y_3^d & z_3^d & 1 \\ y_4^d & z_4^d & 1 \end{bmatrix} \begin{bmatrix} b \\ c \\ d \end{bmatrix} = \begin{bmatrix} a_1^d \\ a_2^d \\ a_3^d \\ a_4^d \end{bmatrix} = \boldsymbol{b} \tag{12}$$

is found by solving the normal system $\boldsymbol{A^T Ax = A^T b}$ in order to minimize (11) [30]. The least-square regression may also help to filter the DVL data from noise.

Remark 6. For three or more DVL beams to give valid echoes of the net pen, the proposed method requires the net pen to be in-sight of the DVL cone and that three or more beam paths are uninterrupted. Notice, however, that the method does not require for the DVL to be perpendicular to the net pen, as there is no guarantee that the net pen will be perpendicular to the DVL. Because the ROV is passively stable in roll and pitch and the net pen constructed of vertical net walls, the DVL net pen should be in-sight of the DVL, even if the DVL is not perfectly perpendicular to the net pen.

B. Calculation of the Desired Heading

For the ROV yaw angle to be pointed directly towards the net pen approximation, the ROV heading will have to be aligned with the projection of the normal vector to f onto the North-East plane, see Fig. 5 and 6.

In the $\{d\}$ reference frame, the normal vector to f is given by

$$\boldsymbol{n}^d \triangleq \begin{bmatrix} -1 & b & c \end{bmatrix}^T, \tag{13}$$

while it can be represented in $\{n\}$ by

$$\boldsymbol{n}^n = \boldsymbol{R}(\psi)\left(\boldsymbol{R}_b^d(\boldsymbol{\Theta}_{db})\right)^T \boldsymbol{n}^d \tag{14}$$

Furthermore, let the vector $\boldsymbol{Z}^n \triangleq [0,0,1]^T$ denote the normal vector to the North-East plane expressed in $\{n\}$. The projection of $\boldsymbol{n}^n$ onto the North-East plane is then given by

$$\boldsymbol{n}^n_{\text{projection}} = \begin{bmatrix} x^n_{\text{projection}} \\ y^n_{\text{projection}} \\ 0 \end{bmatrix} = -\boldsymbol{Z}^n \times \boldsymbol{n}^n \times \boldsymbol{Z}^n \tag{15}$$

The negative sign in Equation (15) makes $\boldsymbol{n}^n_{\text{projection}}$ point from the ROV towards the approximated net pen, as shown in Fig. 5.

Finally, define

$$\psi_d \triangleq \text{atan2}(\text{y}^{\text{n}}_{\text{projection}}, \text{x}^{\text{n}}_{\text{projection}}) \tag{16}$$

which denotes the angle between the north-axis and $\boldsymbol{n}^n_{\text{projection}}$. This angle will be the desired heading angle transferred to the motion control system.

C. ROV Distance Relative to the Approximated Net Pen

The distance between the CO and the plane approximation can be calculated from the inner-product between the unit normal vector to f and any vector from the CO to the plane. The unit normal vector to the plane is given by

$$\boldsymbol{n}^d_{\text{unit}} = \frac{\boldsymbol{n}^d}{||\boldsymbol{n}^d||_2} = \frac{1}{\sqrt{1+b^2+c^2}} \begin{bmatrix} -1 \\ b \\ c \end{bmatrix} \tag{17}$$

As for the other vector, one choice is the vector from the CO to the point where the x-axis in $\{d\}$ intersects the plane. Revisiting the equation for the plane approximation, the equation can be rewritten as

$$f(x,y,z) = -(x-x_0) + b(y-y_0) + c(z-z_0), \tag{18}$$

where $\boldsymbol{p}_0^d = [x_0^d, y_0^d, z_0^d]^T$ is the point where x^d intersects the plane and $d = x_0 - by_0 - cz_0$. The vector from the CO to $\boldsymbol{p}_0^d$ is then given by

$$\boldsymbol{v}^d = \boldsymbol{r}^b_{b/\text{dvl}} + \boldsymbol{p}_0^d = \begin{bmatrix} x^d_{b/\text{dvl}} + x_0^d \\ y^d_{b/\text{dvl}} + y_0^d \\ z^d_{b/\text{dvl}} + z_0^d \end{bmatrix} \tag{19}$$

Finally, the distance between the ROV and the plane approximation is given by

$$\begin{aligned} d_{b/\text{net}} &\triangleq \left|(\boldsymbol{v}^d)^T \boldsymbol{n}^d_{\text{unit}}\right| \\ &= \frac{\left|-x^d_{b/\text{dvl}} + by^d_{b/\text{dvl}} + cz^d_{b/\text{dvl}} - d\right|}{\sqrt{1+b^2+c^2}} \end{aligned} \tag{20}$$

VI. Control System

In this section, we propose a control system that enables ROV path following of continuous paths, including both straight-line and curved paths. Combined with the net pen approximation method in Section V, this will allow autonomous net following. However, as the proposed control system is not limited to the case of net following, the control system is presented in a more generalized context, including any continuous two-dimensional path.

The proposed control strategy consists of four components; a LOS guidance law for fully-actuated vehicles, an adaptive yaw controller to control the heading of the vehicle, and adaptive surge and sway controllers for tracking of the desired velocities provided by the guidance law. The stability analysis of the resulting closed-loop system with the guidance law and control laws in a cascade is given in Section VII.

A. Control Objectives

Consider a two-dimensional desired path $\mathcal{P}$ in $\mathcal{C}^2$ which can be parameterized as $(x_p(\theta), y_p(\theta))$, where θ is the path variable. The control system should make the ROV follow $\mathcal{P}$ with a desired constant speed $U_d > 0$ and with the heading angle converging to some desired heading ψ_d.

For any point $(x_p(\theta), y_p(\theta))$ along the path, the path-tangential reference frame is rotated by the path-tangential angle:

$$\gamma_p(\theta) = \text{atan2}\left(\text{y}_\text{p}'(\theta), \text{x}_\text{p}'(\theta)\right) \tag{21}$$

about the North-East reference frame. Furthermore, the orthogonal distance to the path-tangential reference frame at any point $(x_p(\theta), y_p(\theta))$ is given by the crosstrack error:

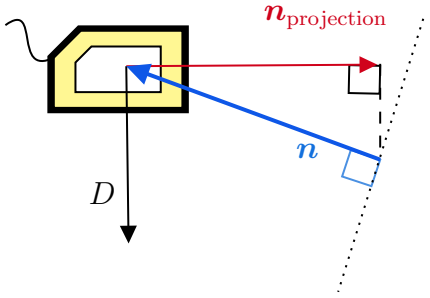

Fig. 5. Vertical projection of the ROV position relative to the plane approximation, where $\boldsymbol{n}$ is the normal vector to the plane approximation and $\boldsymbol{n}_{\text{projection}}$ is its projection onto the North-East plane.

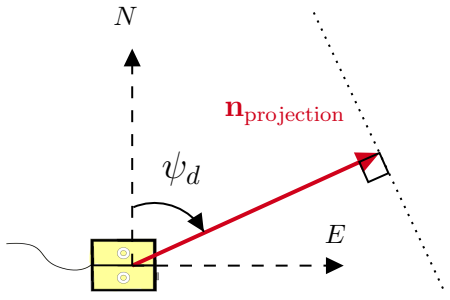

Fig. 6. Horizontal projection of the ROV position relative to the plane approximation, where ψ_d is the angle from the north axis to $\boldsymbol{n}_{\text{projection}}$.

$$y_e(\theta) = -\left(x - x_p(\theta)\right)\sin\left(\gamma_p(\theta)\right) + \left(y - y_p(\theta)\right)\cos\left(\gamma_p(\theta)\right) \tag{22}$$

For open curves, Definition 1 in [21] states that there exists a unique solution of (22) obtained by minimizing θ.

We are now ready to formalize the control objectives:

$$\lim_{t\to\infty} y_e(t) = 0 \tag{23}$$

$$\lim_{t\to\infty} U(t) - U_d = 0 \tag{24}$$

$$\lim_{t\to\infty} \left(\psi(t) - \psi_d(t)\right) = 0 \tag{25}$$

For net following, the desired path is along the net pen with a desired distance, d_d, between the ROV and the net. The crosstrack error can be calculated directly from $y_e = d_{b/\text{net}} - d_d$.

B. Guidance Law

The LOS guidance law is based upon calculating a course angle which will achieve path following properties if successfully tracked and is defined by the following equation [29, Ch. 10.3.2]:

$$\chi_{\text{LOS}} \triangleq \gamma_p - \arctan\left(\frac{y_e}{\Delta}\right) \tag{26}$$

where χ_{LOS} is the desired course angle and Δ is a positive constant known as the lookahead distance.

The vehicle course angle is defined by $\chi \triangleq \psi + \beta$, i.e. the sum of the heading angle, ψ, and the crab angle $\beta \triangleq \arctan(v/u)$. For underactuated vessels, path following is achieved by controlling the heading to follow $\psi = \chi_{\text{LOS}} - \beta$. In the presence of disturbances and with β unknown, adding integral action to (26) is an often-used technique [20], [23].

The guidance law presented in this paper is an extension of the LOS guidance law to fully-actuated vehicles. The proposed guidance law is able to minimize the crosstrack error independently of the vehicle heading ψ, by utilizing that the ROV is fully-actuated in the horizontal plane. This is done by controlling the crab angle β, which is in turn achieved by controlling the surge and sway velocities u, v. The inputs to the guidance law are the vehicle heading ψ, the path-tangential angle γ_p and the crosstrack error y_e, while the outputs are the desired surge velocity u_d and sway velocity v_d.

We now propose the guidance law:

$$\begin{aligned} u_d \triangleq& U_d \cos\left(-\psi + \chi_{\text{LOS}}\right) \\ =& U_d \cos\left(-\psi + \gamma_p - \arctan\left(\frac{y_e}{\Delta}\right)\right) \\ v_d \triangleq& U_d \sin\left(-\psi + \chi_{\text{LOS}}\right) \\ =& U_d \sin\left(-\psi + \gamma_p - \arctan\left(\frac{y_e}{\Delta}\right)\right) \end{aligned} \tag{27}$$

that makes the vehicle follow the path $\mathcal{P}$, where $U_d \triangleq \sqrt{u_d^2 + v_d^2}$ is the desired speed.

Remark 7. For the specific case of net pen inspection addressed in this paper, the desired path to follow is defined based on the net pen approximation obtained from the DVL in a dynamical real-time fashion as described in Section V. Therefore, the path and hence γ_p are defined from the signal ψ_d given in (16), which can be easily rendered class $\mathcal{C}^2$ via, for instance, appropriate reference models [29, Ch. 10.2.1]. This yields $\gamma_p = \psi_d + \pi/2$ when the ROV is directed to traverse the net pen in its starboard direction, while net pen following in the port direction yields $\gamma_p = \psi_d - \pi/2$. For the generic case, γ_p and ψ_d are independent of each other.

C. Surge, Sway and Yaw Control

To track the desired surge velocity $u_d(t)$, the following control law is proposed:

$$\begin{aligned} \tau_u \triangleq& -\frac{m_{22}}{m_{11}} vr + \frac{d_{11}}{m_{11}} u_d - \boldsymbol{\phi}_u^T(\psi, r)\hat{\boldsymbol{\theta}}_u + \dot{u}_d - k_u(u - u_d) \\ & \dot{\hat{\boldsymbol{\theta}}}_u = \gamma_u \boldsymbol{\phi}_u(\psi, r)(u - u_d) \end{aligned} \tag{28}$$

where $k_u > 0$ is a constant controller gain, $\gamma_u > 0$ is a constant adaptation gain and $\hat{\boldsymbol{\theta}}_u$ is an estimate of $\boldsymbol{\theta}_u$. The proposed control law is an adaptive feedback-linearizing P-controller.

Similarly, the control law for tracking of the desired sway velocity $v_d(t)$ is

$$\begin{aligned} \tau_v \triangleq& \frac{m_{11}}{m_{22}} ur + \frac{d_{22}}{m_{22}} v_d - \boldsymbol{\phi}_v^T(\psi, r)\hat{\boldsymbol{\theta}}_v + \dot{v}_d - k_v(v - v_d) \\ & \dot{\hat{\boldsymbol{\theta}}}_v = \gamma_v \boldsymbol{\phi}_v(\psi, r)(v - v_d) \end{aligned} \tag{29}$$

where $k_v > 0$ is a constant controller gain, $\gamma_v > 0$ is a constant adaptation gain and $\hat{\boldsymbol{\theta}}_v$ is an estimate of $\boldsymbol{\theta}_v$. Again, this is an adaptive feedback-linearizing P-controller.

Finally, to solve the yaw tracking control problem, the following control law is proposed:

$$\begin{aligned} \tau_r \triangleq& \frac{d_{33}}{m_{33}} r - \frac{m_{11} - m_{22}}{m_{33}} uv - \boldsymbol{\phi}_r^T(u, v, \psi)\hat{\boldsymbol{\theta}}_r + \ddot{\psi}_d \\ & - (k_\psi + \lambda k_r)(\psi - \psi_d) - (k_r + \lambda)(r - \dot{\psi}_d) \\ \dot{\hat{\boldsymbol{\theta}}}_r =& \gamma_r \boldsymbol{\phi}_r(u, v, \psi)\left[(r - \dot{\psi}_d) + \lambda(\psi - \psi_d)\right] \end{aligned} \tag{30}$$

where $k_\psi, k_r, \lambda > 0$ are constant controller gains, $\gamma_r > 0$ is a constant adaptation gain and $\hat{\boldsymbol{\theta}}_r$ an estimate of $\boldsymbol{\theta}_r$. The control law is an adaptive feedback-linearizing PD-controller.

Remark 8. The control laws presented in (28)-(30) are feedback-linearizing controllers. If the model (7) suffers from high model uncertainty, other control design approaches such as sliding mode control [31],[32],[33],[34] or adaptive control designs which address model uncertainty [35],[36] should be considered.

Remark 9. Damping in surge and sway is not canceled, to provide some robustness to model uncertainties and environmental disturbances.

The suggested control laws are similar to the surge and yaw control laws suggested in [20]; compared to [20], in this paper sway control has been added as well.

In the following, we will show that the proposed controllers (28)-(30) make the surge velocity, sway velocity and yaw angle and rate converge to their references. This result will be utilized in Section VII to show that the complete closed-loop system (7) with guidance law (27) and surge, sway and yaw controllers (28)-(30) satisfies the control objectives (23)-(25).

Define the following tracking errors:

$$\begin{aligned}\tilde{u} &\triangleq u - u_d \\ \tilde{v} &\triangleq v - v_d \\ \tilde{\psi} &\triangleq \psi - \psi_d \\ \dot{\tilde{\psi}} &\triangleq r - \dot{\psi}_d\end{aligned} \tag{31}$$

and estimation errors:

$$\begin{aligned}\tilde{\boldsymbol{\theta}}_u &\triangleq \hat{\boldsymbol{\theta}}_u - \boldsymbol{\theta}_u \\ \tilde{\boldsymbol{\theta}}_v &\triangleq \hat{\boldsymbol{\theta}}_v - \boldsymbol{\theta}_v \\ \tilde{\boldsymbol{\theta}}_r &\triangleq \hat{\boldsymbol{\theta}}_r - \boldsymbol{\theta}_r\end{aligned} \tag{32}$$

Finally, define the vector of errors:

$$\boldsymbol{\xi} \triangleq [\tilde{u}, \tilde{v}, \tilde{\psi}, \dot{\tilde{\psi}}, \tilde{\boldsymbol{\theta}}_u, \tilde{\boldsymbol{\theta}}_v, \tilde{\boldsymbol{\theta}}_r]^T \tag{33}$$

Inserting the proposed adaptive control laws (28)-(30) in (7c)-(7f) we obtain the following closed-loop error dynamics:

$$\begin{aligned}\dot{\tilde{u}} &= -\left(k_u + \frac{d_{11}}{m_{11}}\right)\tilde{u} - \boldsymbol{\phi}_u^T(\psi, r)\tilde{\boldsymbol{\theta}}_u \\ \dot{\tilde{v}} &= -\left(k_v + \frac{d_{22}}{m_{22}}\right)\tilde{v} - \boldsymbol{\phi}_v^T(\psi, r)\tilde{\boldsymbol{\theta}}_v \\ \ddot{\tilde{\psi}} &= -\left(k_\psi + \lambda k_r\right)\tilde{\psi} - \left(k_r + \lambda\right)\dot{\tilde{\psi}} - \boldsymbol{\phi}_r^T(u, v, \psi)\tilde{\boldsymbol{\theta}}_r \\ \dot{\tilde{\boldsymbol{\theta}}}_u &= \gamma_u \boldsymbol{\phi}_u(\psi, r)\tilde{u} \\ \dot{\tilde{\boldsymbol{\theta}}}_v &= \gamma_v \boldsymbol{\phi}_v(\psi, r)\tilde{v} \\ \dot{\tilde{\boldsymbol{\theta}}}_r &= \gamma_r \boldsymbol{\phi}_r(u, v, \psi)\left(\dot{\tilde{\psi}} + \lambda\tilde{\psi}\right)\end{aligned} \tag{34}$$

Proposition 1. *Given an underwater vehicle described by* (7c)-(7f)*. If Assumptions 1-7 hold, the proposed control laws* (28)-(30) *with adaptive laws ensure that* $\boldsymbol{\xi} = \mathbf{0}$ *is a uniformly globally stable (UGS) equilibrium point of* (34) *and that* $\tilde{\psi} \to 0, \dot{\tilde{\psi}} \to 0, \tilde{u} \to 0$ *and* $\tilde{v} \to 0$ *asymptotically as* $t \to \infty$*.*

Proof. In the first part of the proof, we shall show that $\boldsymbol{\xi} = \mathbf{0}$ is a UGS equilibrium point of (34). Define the tracking error variable $s \triangleq \dot{\tilde{\psi}} + \lambda\tilde{\psi}$. Consider the positive definite radially unbounded functions

$$\begin{aligned}V_\psi(\tilde{\psi}, s, \tilde{\theta}_r) &= \frac{1}{2}k_\psi\tilde{\psi}^2 + \frac{1}{2}s^2 + \frac{1}{2\gamma_r}\tilde{\boldsymbol{\theta}}_r^T\tilde{\boldsymbol{\theta}}_r \\ V_u(\tilde{u}, \tilde{\theta}_u) &= \frac{1}{2}\tilde{u}^2 + \frac{1}{2\gamma_u}\tilde{\boldsymbol{\theta}}_u^T\tilde{\boldsymbol{\theta}}_u \\ V_v(\tilde{v}, \tilde{\theta}_v) &= \frac{1}{2}\tilde{v}^2 + \frac{1}{2\gamma_v}\tilde{\boldsymbol{\theta}}_v^T\tilde{\boldsymbol{\theta}}_v\end{aligned} \tag{35}$$

Let $V = V_\psi + V_u + V_v$ be a Lyapunov function candidate for (34). Its time derivative is negative semi-definite:

$$\begin{aligned}\dot{V} =& -\lambda k_\psi\tilde{\psi}^2 - k_r s^2 - \left(k_u + \frac{d_{11}}{m_{11}}\right)\tilde{u}^2 \\ &- \left(k_v + \frac{d_{22}}{m_{22}}\right)\tilde{v}^2 \leq 0\end{aligned} \tag{36}$$

Hence, the origin $\boldsymbol{\xi} = \mathbf{0}$ is uniformly globally stable.

We now move on to prove that the tracking errors $\tilde{\psi}, \dot{\tilde{\psi}}, \tilde{u}$ and $\tilde{v}$ converge to their origins asymptotically as $t \to \infty$. Since the time derivative $\dot{V}$ is not negative definite, we utilize Barbalat's lemma [37, Lemma 8.2]:

Since $V > 0$ and $\dot{V} \leq 0$, it follows that, for all $t \geq t_0$,

$$0 < V(t) \leq V(t_0) < \infty \tag{37}$$

Hence,

$$\lim_{t\to\infty}\int_0^t \dot{V}(t)dt = \lim_{t\to\infty} V(t) - V(t_0) \tag{38}$$

exists and is finite. Furthermore, the second order time-derivative of $V(t)$ is given by

$$\begin{aligned}\ddot{V}(t) =& -2k_\psi\tilde{\psi}\dot{\tilde{\psi}} - 2k_r(\dot{\tilde{\psi}} + \lambda\tilde{\psi})(\ddot{\tilde{\psi}} + \lambda\dot{\tilde{\psi}}) \\ &- 2\left(k_u + \frac{d_{11}}{m_{11}}\right)\tilde{u}\dot{\tilde{u}} - 2\left(k_v + \frac{d_{22}}{m_{22}}\right)\tilde{v}\dot{\tilde{v}} \\ =& -2k_\psi\tilde{\psi}\dot{\tilde{\psi}} \\ &-2k_r(\dot{\tilde{\psi}} + \lambda\tilde{\psi})\left(-(k_\psi + \lambda k_r)\tilde{\psi} - k_r\dot{\tilde{\psi}} - \boldsymbol{\phi}_r^T\tilde{\boldsymbol{\theta}}_r\right) \\ &-2\left(k_u + \frac{d_{11}}{m_{11}}\right)\left(-\left(k_u + \frac{d_{11}}{m_{11}}\right)\tilde{u}^2 - \boldsymbol{\phi}_u^T\tilde{\boldsymbol{\theta}}_u\tilde{u}\right) \\ &-2\left(k_v + \frac{d_{22}}{m_{22}}\right)\left(-\left(k_v + \frac{d_{22}}{m_{22}}\right)\tilde{v}^2 - \boldsymbol{\phi}_v^T\tilde{\boldsymbol{\theta}}_v\tilde{v}\right)\end{aligned} \tag{39}$$

Since the origin $\boldsymbol{\xi} = \mathbf{0}$ is UGS, it follows that u, v, r are globally uniformly bounded and thus $\boldsymbol{\phi}_u, \boldsymbol{\phi}_v, \boldsymbol{\phi}_r$ are globally uniformly bounded by their definition (App. A), i.e. there exists constants $c_1, c_2, c_3 > 0$ such that $|\boldsymbol{\phi}_u| < c_1, |\boldsymbol{\phi}_v| < c_2, |\boldsymbol{\phi}_r| < c_3\ \forall t \geq t_0$. Then, since all variables $\boldsymbol{\xi}, \boldsymbol{\phi}_u, \boldsymbol{\phi}_v, \boldsymbol{\phi}_r$ on the right hand side of Eq. (39) are globally uniformly bounded, it follows that also $\ddot{V}(t)$ is globally uniformly bounded, i.e., there exists a constant $c_4 > 0$ such that $|\ddot{V}(t)| < c_4\ \forall t \geq t_0$. The bound on $\ddot{V}(t)$ implies that $\dot{V}(t)$ is uniformly continuous in t. Hence, by Barbalat's lemma [37, Lemma 8.2], we have that $\dot{V}(t) \to 0$ asymptotically as $t \to \infty$. By (36), the asymptotic convergence of $\dot{V}$ to zero ensures that $\tilde{\psi} \to 0, s \to 0, \tilde{u} \to 0$ and $\tilde{v} \to 0$ asymptotically as $t \to \infty$. Finally, as $s = \dot{\tilde{\psi}} + \lambda\tilde{\psi}$, the asymptotic convergence of s and $\tilde{\psi}$ to zero implies the asymptotic convergence of $\dot{\tilde{\psi}}$ to zero. □

Remark 10. The asymptotic convergence of u, v to u_d, v_d implies the asymptotic convergence of U to U_d, as $U = \sqrt{u^2 + v^2}$ and $U_d = \sqrt{u_d^2 + v_d^2}$ by definition.

Remark 11. The convergence of $\tilde{\boldsymbol{\theta}}_r, \tilde{\boldsymbol{\theta}}_u, \tilde{\boldsymbol{\theta}}_v$ to their origins cannot be shown, as persistently exciting regressors $\boldsymbol{\phi}_r(u, v, \psi), \boldsymbol{\phi}_u(\psi, r), \boldsymbol{\phi}_v(\psi, r)$ would be necessary conditions [38, Ch. 4.3.4].

VII. Stability Analysis of the Cascaded System

This section presents the stability analysis of the closed-loop system of (7) with the guidance law (27) and control laws (28)-(30). Using cascaded system theory we can show that the closed-loop system will satisfy the control objectives in Section VI-A.

Theorem 1. *Given an underwater vehicle described by* (7)*. If Assumptions 1-7 hold, the proposed guidance law* (27) *and control laws* (28)-(30) *ensure that* $y_e \to 0$ *asymptotically as* $t \to \infty$.

Proof. The dynamic of the crosstrack error is given by [21]

$$\begin{aligned}\dot{y}_e =& -\dot{x}\sin(\gamma_p) + \dot{y}\cos(\gamma_p)\\ =& -(u\cos(\psi) - v\sin(\psi))\sin(\gamma_p)\\ &+ (u\sin(\psi) + v\cos(\psi))\cos(\gamma_p)\\ =& u(\sin(\psi)\cos(\gamma_p) - \cos(\psi)\sin(\gamma_p))\\ &+ v(\sin(\psi)\sin(\gamma_p) + \cos(\psi)\cos(\gamma_p))\\ =& (\tilde{u}+u_d)\sin(\psi-\gamma_p) + (\tilde{v}+v_d)\cos(\psi-\gamma_p)\end{aligned} \tag{40}$$

This can be written as

$$\begin{aligned}\dot{y}_e =& U_d \sin\left(\psi - \gamma_p + \arctan\left(\frac{v_d}{u_d}\right)\right)\\ &+\tilde{u}\sin(\psi-\gamma_p) + \tilde{v}\cos(\psi-\gamma_p)\end{aligned} \tag{41}$$

Choosing the guidance law according to (27) yields

$$\begin{aligned}\dot{y}_e =& U_d \sin\left(-\arctan\left(\frac{y_e}{\Delta}\right)\right) + \tilde{u}\sin(\psi-\gamma_p)\\ &+ \tilde{v}\cos(\psi-\gamma_p)\\ =& -\frac{U_d}{\sqrt{\Delta^2+y_e^2}}y_e + \tilde{u}\sin(\psi-\gamma_p) + \tilde{v}\cos(\psi-\gamma_p)\end{aligned} \tag{42}$$

which can be written as

$$\dot{y}_e = f_1(t, y_e) + \boldsymbol{g}(t, \tilde{\psi}, \gamma_p)\boldsymbol{\xi} \tag{43}$$

where

$$f_1(t, y_e) \triangleq -\frac{U_d}{\sqrt{\Delta^2+y_e^2}}y_e \tag{44}$$

$$\begin{aligned}&\boldsymbol{g}(t, \tilde{\psi}, \gamma_p) \triangleq\\ &\begin{bmatrix}\sin(\tilde{\psi}+\psi_d(t)-\gamma_p) & \cos(\tilde{\psi}+\psi_d(t)-\gamma_p) & \mathbf{0}_{1x11}\end{bmatrix}\end{aligned} \tag{45}$$

We note that (34) and (43) constitute a cascaded system where the nominal system

$$\dot{y}_e = f_1(t, y_e) \tag{46}$$

is perturbed by the error dynamics (34) through the term $\boldsymbol{g}(t, \tilde{\psi}, \gamma_p)\boldsymbol{\xi}$.

Lemma 1. *The origin of the nominal system* (46) *is uniformly globally asymptotically stable (UGAS) and uniformly semi-globally exponentially stable (USGES).*

Proof. The proof is given in [21]. □

Fig. 7. Argus Mini ROV, courtesy of Argus Remote Systems AS.

It now remains to analyze the cascaded system (34), (43). From (45), it is trivial to see that $\boldsymbol{g}(t, \tilde{\psi}, \gamma_p)$ is globally bounded. Furthermore, since the origin of $\boldsymbol{\xi}$ is UGS and $\tilde{u}, \tilde{v}$ converges to zero asymptotically as $t \to \infty$, we have that the perturbing term $\boldsymbol{g}(t, \tilde{\psi}, \gamma_p)\boldsymbol{\xi}$ is globally bounded and vanishing.

Since the nominal system (46) is UGAS and $\boldsymbol{g}(t, \tilde{\psi}, \gamma_p)\boldsymbol{\xi}$ is bounded, every trajectory of y_e will be bounded. Finally, since the area of attraction of the nominal system (46) is global and the perturbing term $\boldsymbol{g}(t, \tilde{\psi}, \gamma_p)\boldsymbol{\xi}$ is vanishing, the crosstrack error y_e converges asymptotically to zero [39]. □

VIII. Simulations and Experiments

This section presents the results from simulations and experiments of the proposed net pen geometry approximation and control system. Results from both preliminary basin trials and full-scale trials at an aquaculture fish farm are presented. The simulations show the performance of the proposed net pen geometry approximation and control system under ideal conditions, while the basin trials serve as a first proof-of-concept where hardware and sensors are first included in the control loop. Finally, sea trials in a full scale aquaculture facility are executed under realistic operational conditions.

A. Vehicle Model

The vehicle used during the experiments was a 90 kg Argus Mini ROV with dimensions $[0.9\text{m}, 0.65\text{m}, 0.6\text{m}]^T$. The ROV is illustrated in Figure 7. In order to have simulations that can be directly compared to the experiments, the vehicle simulation model is implemented as close as possible to the Argus Mini ROV, while still satisfying Assumptions 1-7.

The Argus Mini has 4 horizontal thrusters, as well as 2 vertical thrusters. The arrangement of the horizontal thrusters is depicted in Figure 8. The horizontal thrusters have azimuth angles of $\pm 35°$, giving actuation in surge, sway and yaw. The vehicle state matrices, including the thruster allocation matrix $\boldsymbol{B}$, are given in Appendix B. Furthermore, in simulations, the thrusters have been saturated and their rate limited in order to achieve a realistic response.

The current velocity components during simulations are $[V_x, V_y]^T = [0, 0.2\text{m/s}]^T$. The DVL is mounted on the front side of the ROV with rotation $\boldsymbol{R}_d^b(\boldsymbol{\Theta}_{db}) = \mathbb{I}_3$. The DVL

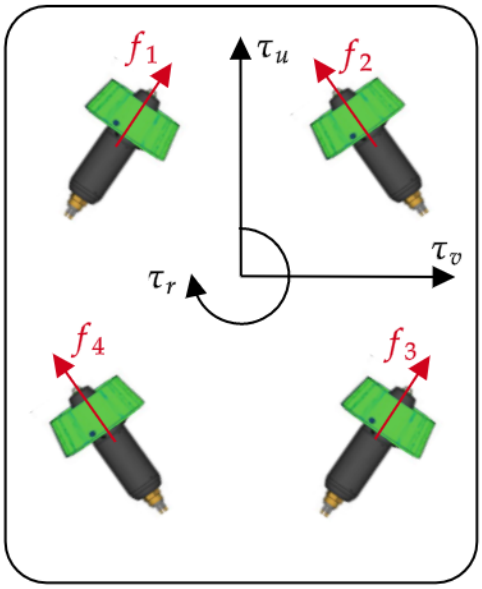

Fig. 8. Horizontal thruster configuration on Argus Mini ROV.

beam angles are $[\beta_1, \beta_2, \beta_3, \beta_4]^T = [45°, 135°, 225°, 315°]^T$ and $\gamma_j = 25°, j \in \{1, 2, 3, 4\}$.

B. Simulations

This subsection presents simulation results for net pen following.

All simulations are run using the FhSim software [40], [41]. FhSim is a software framework hosted by SINTEF Ocean, aimed at time-domain simulations of surface vessels, underwater vehicles and marine structures operating in the fisheries and aquaculture contexts. Furthermore, FhSim can simulate the biomass response to stimuli such as feeding and ocean currents [42], [43], [44], [45], hence making it a unique virtual environment where to simulate interactions between technology and biology.

The net pen simulation model is a static circular net cage and is constructed from a large number of vertices. At the mooring points between the net walls, the edges are sharp. This net pen model is chosen in order to have simulations close to a realistic scenario. Notice, however, that this is not an ideal simulation setting for the net pen approximation method, as the mooring point edges will not be captured by the DVL when inside of the DVL footprint. To study the accuracy of the net pen approximation, we compare the distance $d_{b/\text{net}}$ between the CO and the net pen approximation against the true distance to the net.

The desired distance d_d to the net is 3 m, while the desired speed U_d is 0.35 m/s. The guidance law lookahead distance is chosen as $\Delta = 1$ m, roughly the same length as the vehicle. In general, a smaller Δ yields more aggressive steering. A guideline for surface vessel path following is to choose Δ two times the length of the vessel. However, due to its thruster configuration and small inertia, the ROV can handle a more aggressive lookahead distance, which justifies the parameter choice. Furthermore, the velocity controller gains are chosen as $k_u = 5, k_v = 5$, while the yaw controller gains are chosen as $k_\psi = 1.89, k_r = 0.79$ and $\lambda = 0.79$. The values for k_u and k_v are chosen to give fast responses for accurate velocity control while staying within the actuator constraints. The chosen values for k_ψ, k_r and λ yields a critical damped system when the parameter estimation error $\boldsymbol{\theta}_r$ in (34) is zero. Finally, the adaptation gains are chosen as $\gamma_u = 2, \gamma_v = 2$ and $\gamma_r = 2$.

Figures 9-11 show the simulation results. In accordance with Proposition 1, the surge, sway and yaw controllers ensure that $\psi(t), u(t)$ and $v(t)$ track their reference signals $\psi_d(t), u_d(t), v_d(t)$. Hence, the vehicle speed $U(t)$ converges to the desired speed U_d and the course angle $\chi(t) = \psi(t) + \arctan(v(t)/u(t))$ successfully tracks the desired course angle $\chi_{\text{LOS}}(t)$. As seen in Fig. 11b-11d, the heading angle $\psi(t)$, surge velocity $u(t)$ and sway velocity $v(t)$ require a short transient time to settle to their reference values. Such transients are likely due to the adaptive nature of the controllers, since the initial estimates of the expressions $\boldsymbol{\theta}_r(t), \boldsymbol{\theta}_u(t), \boldsymbol{\theta}_v(t)$ may be wrong. As seen in Fig. 11b, sudden changes in the reference $\psi_d(t)$ lead to small overshoots for the tracking of the yaw tracking. However, as these overshoots are less than 5 degrees, the yaw angle $\psi(t)$ tracks its reference with sufficient precision. The apparent decline after 300 s in Fig. 9e is due to a mapping of angles to the range $[-\pi, \pi]$.

Figure 9a shows that, in accordance with Theorem 1, the crosstrack error $y_e(t)$ converges towards zero. However, as the net pen approximation is updated at each time step, it is possible to observe that the crosstrack error is affected by larger re-evaluations of the net pen approximation. The maximum offsets stemming from re-evaluations are less than 1.3 cm.

Finally, Fig. 9f shows that the approximated distance to the net appears to be a good estimate of the true distance. The DVL beam angles are constant, so the footprint of the DVL increases with the distance to the net. Hence, the accuracy of the net pen geometry approximation varies with the distance to the net and with the roughness of the net pen geometry. The consequence of this can be observed in Figure 9f. Because the DVL footprint decreases when the ROV is moving closer to the net, the estimation error also decreases. Furthermore, the estimation error grows larger at mooring points and vertices. When the crosstrack error $y_e(t)$ has converged towards its origin, the magnitude of the estimation error is less than 6 cm.

C. Basin Trials

This section presents the results from the preliminary trials executed at the indoor SINTEF - NTNU Ocean Basin Laboratory in Trondheim. By conducting the preliminary trials indoors, the ROV could be shielded from environmental disturbances such as wave and current forces, thus providing an ideal environment for initial tests. The goal of the trials was to integrate the DVL and control system, as well as to verify that the net approximation method and guidance law worked in controlled conditions. The tests were done without the presence of waves and currents.

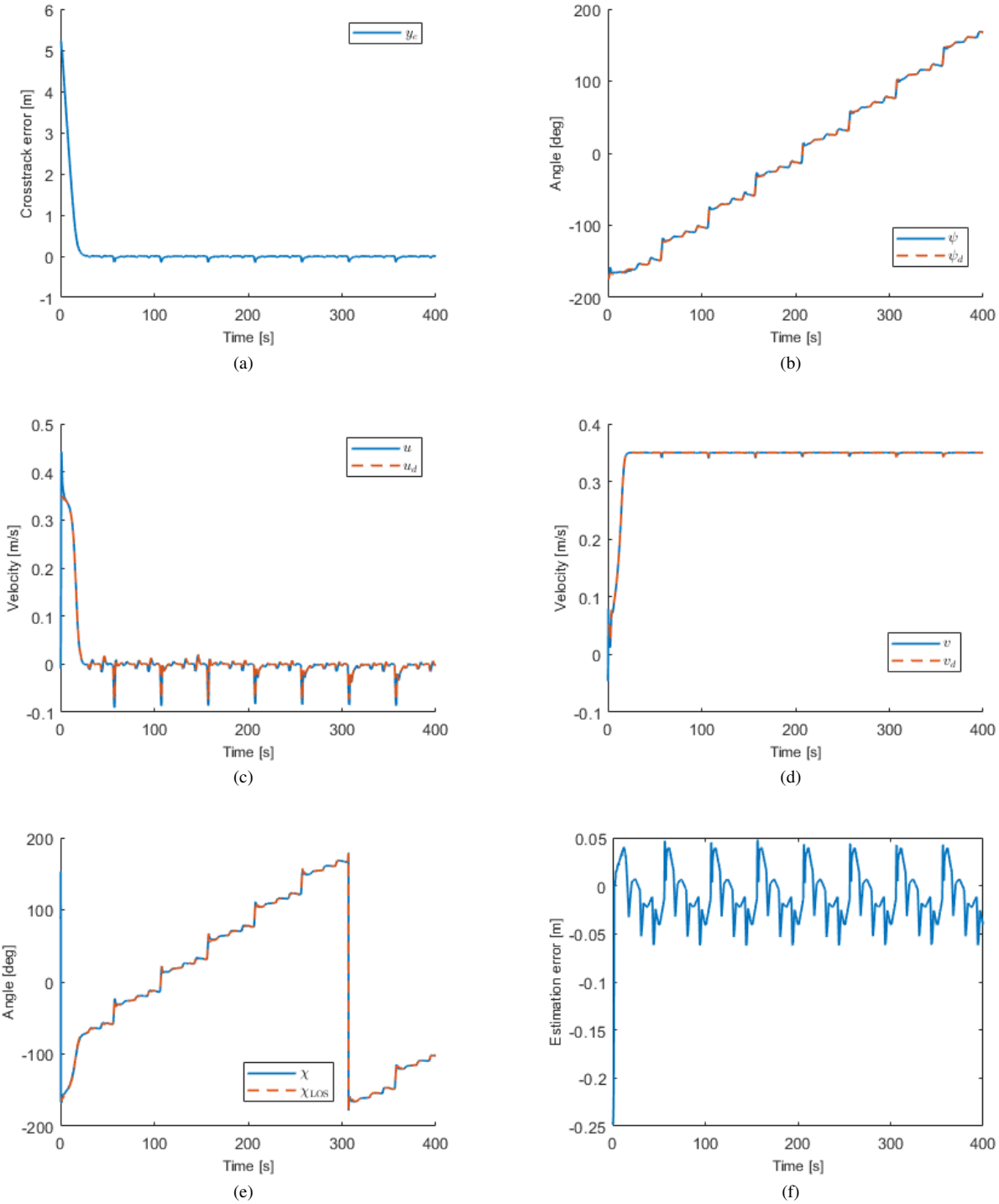

Fig. 9. Simulation results of net pen following in the presence of an unknown ocean current. (a) The crosstrack error y_e. (b) The yaw tracking. (c) The surge velocity tracking. (d) The sway velocity tracking. (e) The tracking of the desired course angle χ_{LOS}, mapped between $[-180, 180]$ degrees. (f) Estimation error of distance to net.

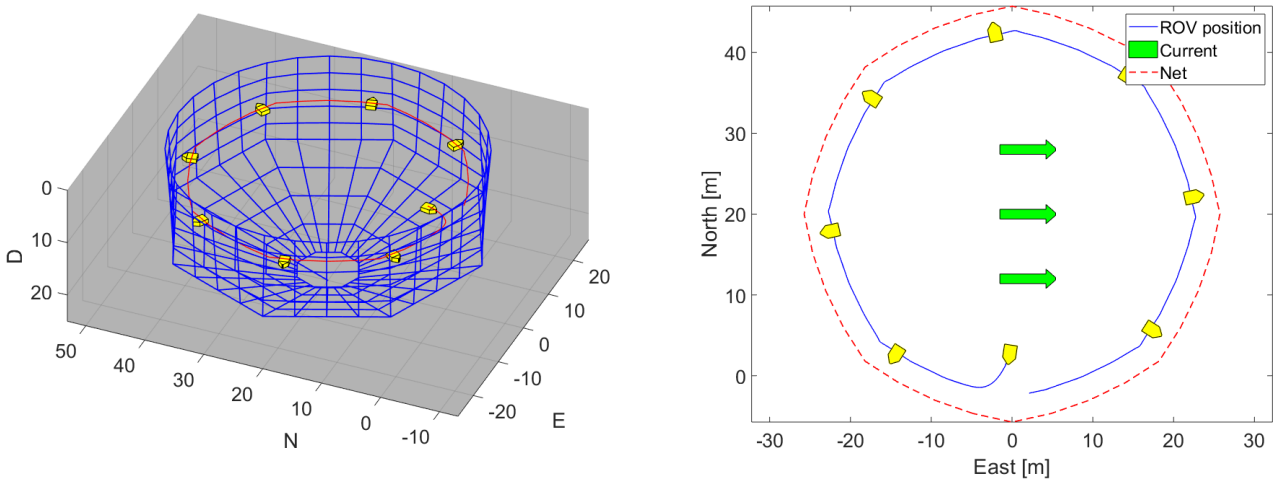

(a) (b)

Fig. 10. Simulation results of net pen following in the presence of an unknown ocean current. (a) Position of the ROV in the 3D space. (b) Position of the ROV in the North-East plane.

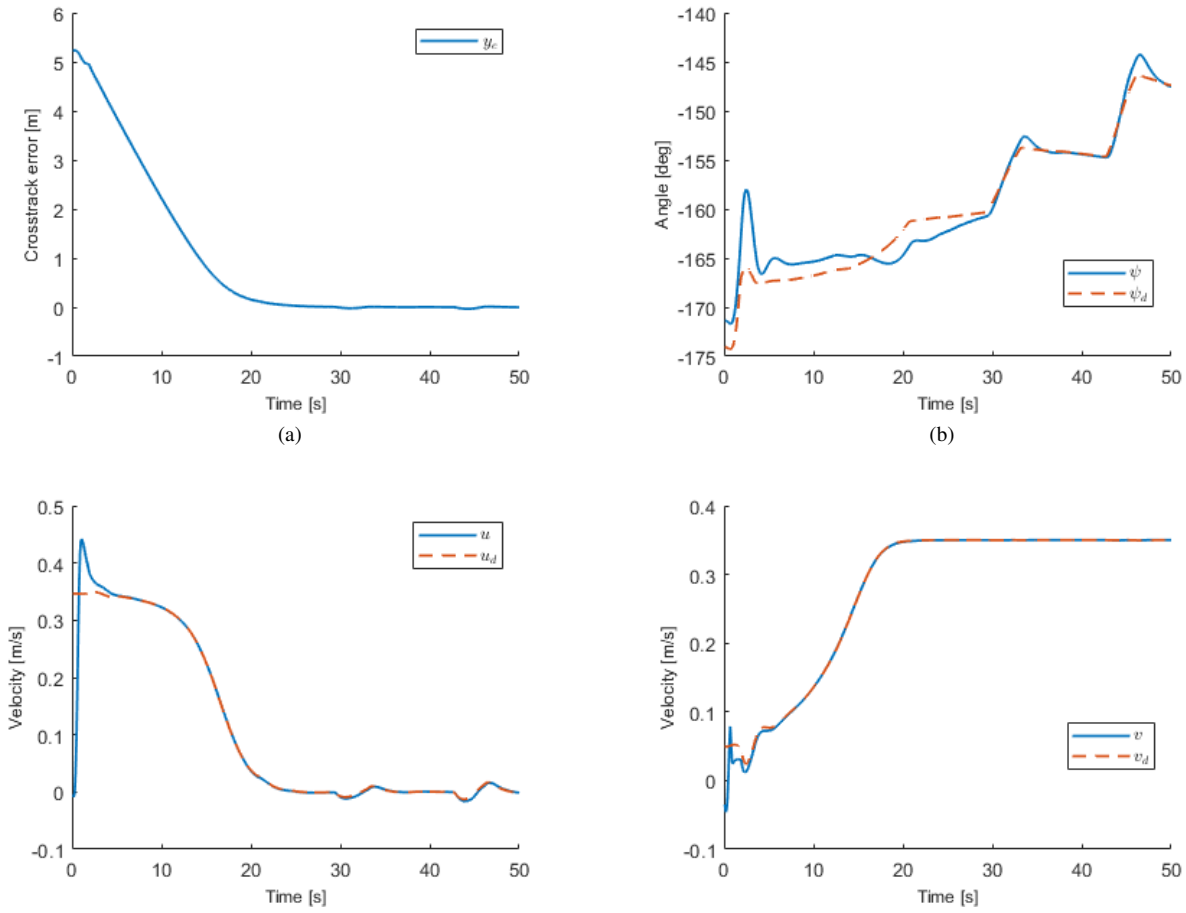

(a) (b) (c) (d)

Fig. 11. Close-up of simulation results of net pen following in the presence of an unknown ocean current. (a) The crosstrack error y_e. (b) The yaw tracking. (c) The surge velocity tracking. (d) The sway velocity tracking.

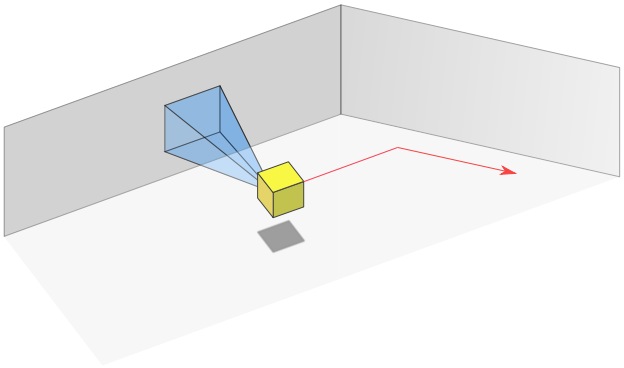

Fig. 12. 3D illustration of the trials at SINTEF - NTNU ocean basin laboratory. The goal was to autonomously follow two wall-segments of the basin using a DVL attached to the front of the ROV.

Fig. 13. SINTEF ACE Rataren, a full-scale laboratory facility designed to develop and test new aquaculture technologies.

The objective was to follow the two wall-segments of the basin, with an obtuse angle at the corner, see Fig. 12. This corner is similar to the corners one might experience at net pen mooring points. During the trials, the desired distance to the basin wall was 2 m, while the desired speed was $U_d = 0.2$ m/s. The lookahead distance was chosen as $\Delta = 1$ m. As the ROV suffers from high model uncertainty, the feedback linearizing control laws were replaced by a classical PID yaw controller and PI velocity controllers.

Figure 15 presents results from the preliminary trials. The trial results supports the theoretical analysis and simulation results. From the DVL measurements, the net approximation method successfully calculates the ROV position and orientation relative to the basin wall. Furthermore, the guidance law and closed-loop control system makes the ROV successfully follow the wall-segments. However, the ROV reacted too late to the corner: in particular, the velocity controllers were not able to follow fast changes in the references, and as a result, the control system was not able to track the desired course angle $\chi_{LOS}(t)$ fast enough. Consequently, the magnitude of the crosstrack error increases after the corner. This highlights the need for better tuning of the surge, sway and yaw controllers.

D. Sea Trials

To validate and analyze the performance of the net pen following method, two extensive sets of sea trials were performed at SINTEF ACE Rataren, a full-scale aquaculture laboratory

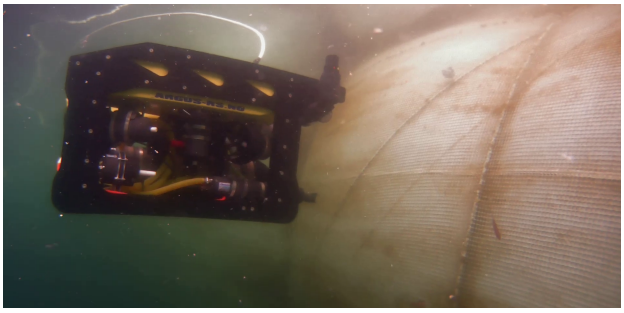

Fig. 14. Underwater footage of the Argus Mini ROV during autonomous net pen following.

located on the western coast of central Norway, see Figure 13. The conditions of the sea trials are comparable to conditions typical for net pen inspections. A circular net pen with a diameter of 50 m was used. The net pen had vertical walls down to a depth of 15 m and a conic shaped bottom with a depth of 12 m. Figure 14 shows a picture of the ROV during the trials. Typical current speeds at Rataren are around 0.3 m/s.

1) Sea Trials 1: In order to limit the scope of the first trial, it was chosen to conduct the experiments in an empty net cage so that the influence of fish on the DVL measurements was eliminated. As salmons might interfere with the transmission and reception of the DVL signals when located in the beam paths, the presence of biomass in the net pen could present a problem to the net pen following algorithm, and this is a subject of further research. Notice that the preliminary results from [17] suggest that the DVL is more likely to retrieve reliable measurements in a net pen with biomass when within a 3 m range of the net.

A Nortek DVL 1000 (1 MHz) was mounted on the bow of the ROV, with a range setting of 6 m and a maximum applied power level. Confirming the results from [17], the DVL successfully interacted with the net pen and the measured beam travel distance was steady and reliable. Loss of measurements could occasionally be experienced, but as they appeared as bursts, they had no significant effect on the performance of the control system. The DVL-measured velocity, however, appeared to be affected by noise, effectively decreasing the performance of the control system. Further filtering of the velocity measurements is needed and is a task of further research.

During the trials, the seas were calm. The desired distance to the net was set to 2 m, while the desired speed was $U_d = 0.2$ m/s. The lookahead distance was chosen as $\Delta = 1$ m. The yaw angle $\psi(t)$ was controlled with a PID controller, while the surge and sway velocities $u(t), v(t)$ were controlled with PI controllers.

Figure 16 shows that the experimental results are in good agreement with the theory and simulation results. The yaw controller successfully tracked its reference signal. With better tuning compared to the basin trials, the performance of the velocity controllers had significantly improved. However, they still did not manage to track their reference signals perfectly. This is probably partly due to disturbances from unmodeled

dynamics and environmental loads. Notice that the theoretical analysis and simulation model assume a constant irrotational current and no induced wave-forces. This will generally not be the case in open sea trials, which therefore serves as a particularly challenging task. Furthermore, due to the measurement noise, the integral gain in the velocity controllers had to be kept low, which made reference tracking challenging. Due to the error in velocity tracking, the vehicle course did not track the desired course $\chi_{\mathrm{LOS}}(t)$ perfectly. The consequence was a small offset in crosstrack error (ca. 20 cm). Nevertheless, the ROV was able to successfully follow the net. The jumps in references are due to the loss of measured DVL beam travel distance.

2) Sea Trials 2: To further validate the net following algorithm, another set of sea trials were performed at SINTEF ACE Rataren. To investigate the performance of the net approximation method with biomass present, the trials were conducted in a net cage with Atlantic salmon. During the trials, the seas appeared moderately rough with considerable current speeds.

As expected, fish intercepting the DVL beams presented a problem for the net following algorithm. When the ROV was more than 3 m away from the net, this was a frequent problem. However, when the ROV was closer to the net, the interference of fish was rare, and the net following method worked as intended.

Figure 17 shows the result from the trials. The desired speed was $U_d = 0.2$ m/s, while the desired distance to the net was $d_d = 1$ m. The lookahead-distance was chosen as $\Delta = 1$ m, the yaw angle $\psi(t)$ was controlled with PID control, and the surge and sway velocities $u(t), v(t)$ were controlled with PI control.

The rougher sea state made it harder to control the states of the ROV, which can be seen in Figure 17. Still, the ROV manages to track the desired course angle $\chi_{\mathrm{LOS}}(t)$ with sufficient precision, as seen in Figure 17e. Therefore, the crosstrack error has a magnitude of less than 0.22m, and the ROV traverses the net with a safe distance. The performance of the net following algorithm is expected to improve with surge, sway and yaw controllers that address model uncertainty and environmental disturbances, which is the subject of ongoing research.

The ROV is equipped with a forward-looking camera and during the trials, the images from the camera appeared clear and steady. This suggests that it is possible to perform autonomous ROV net pen inspections using DVL. Furthermore, it may be possible to further automatize net inspections by including other methods, such as detection of holes by the use of computer vision, or repair operations by the use of robotic manipulators mounted on the ROV.

IX. Conclusion and Future Work

This paper has presented a method for guiding an ROV to autonomously traverse an aquaculture net pen. The first contribution of the paper is a proposed method for approximating the geometry of a local region of the net pen in front of the ROV. By employing a forward-looking DVL, the net pen can be approximated as a plane from the four DVL beam vectors. The ROV orientation and position relative to the net pen approximation were then used as inputs in a LOS guidance law. The main contribution of the proposed guidance law is to minimize the crosstrack error independently of the yaw angle. This is achieved by controlling the surge and sway velocity.

The stability properties of the closed-loop system with the guidance law and proposed velocity controllers were analyzed. In the analysis, the ROV is described by a 3 DOF maneuvering model. When the surge and sway velocity references generated by the guidance law are followed, using adaptive feedback linearizing velocity control laws, it is shown that the guidance law will guide the ROV to the desired path even when a constant, irrotational current is present. Finally, simulations and sea trials demonstrating the performance of the net pen geometry approximation and guidance law were presented.

The proposed method represents a novel approach for autonomous inspections of aquaculture net pens. However, further scientific challenges still need to be addressed, and this is the case of ongoing research. The proposed control laws in Section VI-C do not address model uncertainty. Due to the many cavities and appendages that are typical of ROVs, it is notoriously difficult to accurately model ROVs. Therefore, the proposed feedback linearizing control laws in Section VI-C had to be replaced by traditional PID controllers in the field trials. To achieve proper control of the heading and velocity of the ROV, new control laws that address model uncertainty need to be developed and this is a focus of ongoing research efforts.

Furthermore, the proposed method is dependent on both velocity and distance measurements from the DVL. When interacting with the net pen, the velocity measurements of the DVL appeared to be affected by noise. To enhance the performance of the control system, the velocity measurements should be filtered from noise. Compared to the velocity measurements, the distance measurements appeared less affected by noise. However, fish traveling in the DVL beam paths is a significant source of disturbance to the distance measurements. Fish interception of beams can either yield a non-white noise to the distance measurements or a loss of DVL echo, both critical to the proposed net approximation method. Therefore there is an ongoing research effort towards handling noise from fish interaction, including dead-reckoning of lost measurements.

Appendix A
Functional Expressions

$$\boldsymbol{\phi}_u(\psi, r) = \Bigg[\frac{d_{11}}{m_{11}} \cos\psi - \frac{m_{11}^A - m_{22}^A}{m_{11}} r \sin\psi, \\ \frac{d_{11}}{m_{11}} \sin\psi + \frac{m_{11}^A - m_{22}^A}{m_{11}} r \cos\psi \Bigg]^T \tag{47}$$

$$\boldsymbol{\phi}_v(\psi, r) = \Bigg[-\frac{d_{22}}{m_{22}} \sin\psi - \frac{m_{11}^A - m_{22}^A}{m_{22}} r \cos\psi, \\ \frac{d_{22}}{m_{22}} \cos\psi - \frac{m_{11}^A - m_{22}^A}{m_{22}} r \sin\psi \Bigg]^T \tag{48}$$

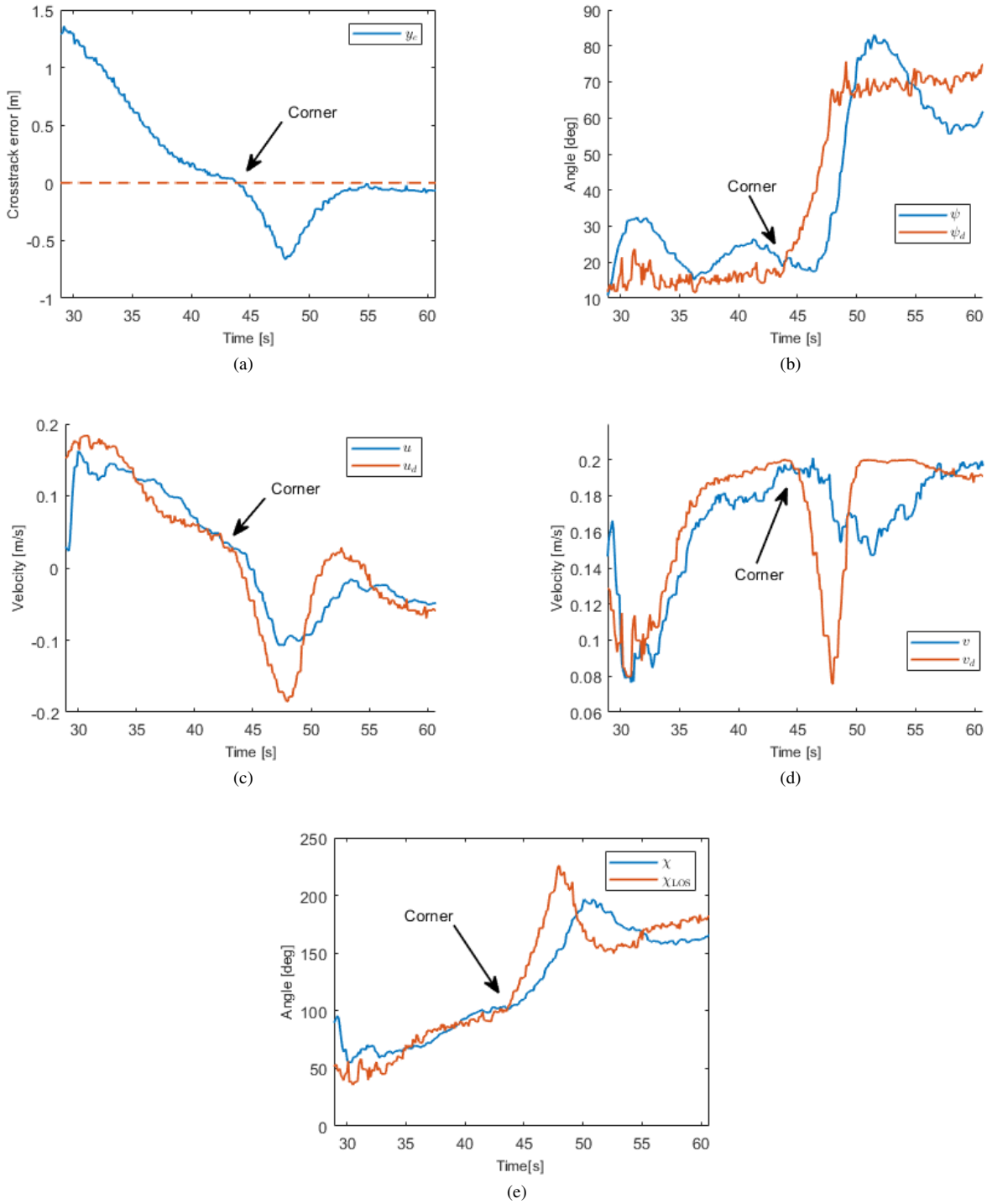

Fig. 15. Basin wall following using DVL. (a) The crosstrack error y_e. (b) The yaw tracking. (c) The surge velocity tracking. (d) The sway velocity tracking. (e) The course angle tracking.

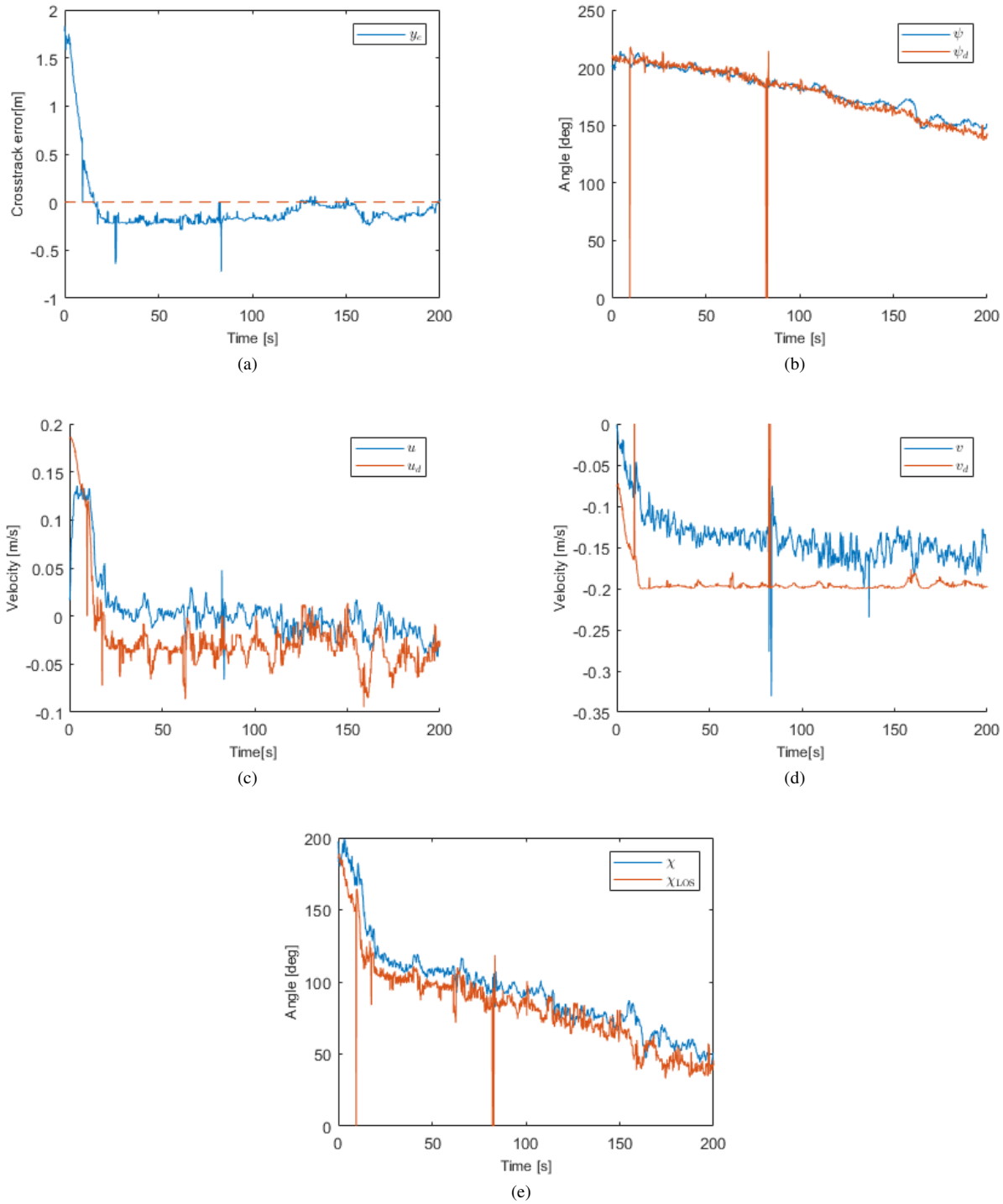

Fig. 16. Experimental results from net pen following trial 1 at SINTEF ACE Rataren. (a) The crosstrack error y_e. (b) The yaw tracking. (c) The surge velocity tracking. (d) The sway velocity tracking. (e) The course angle tracking.

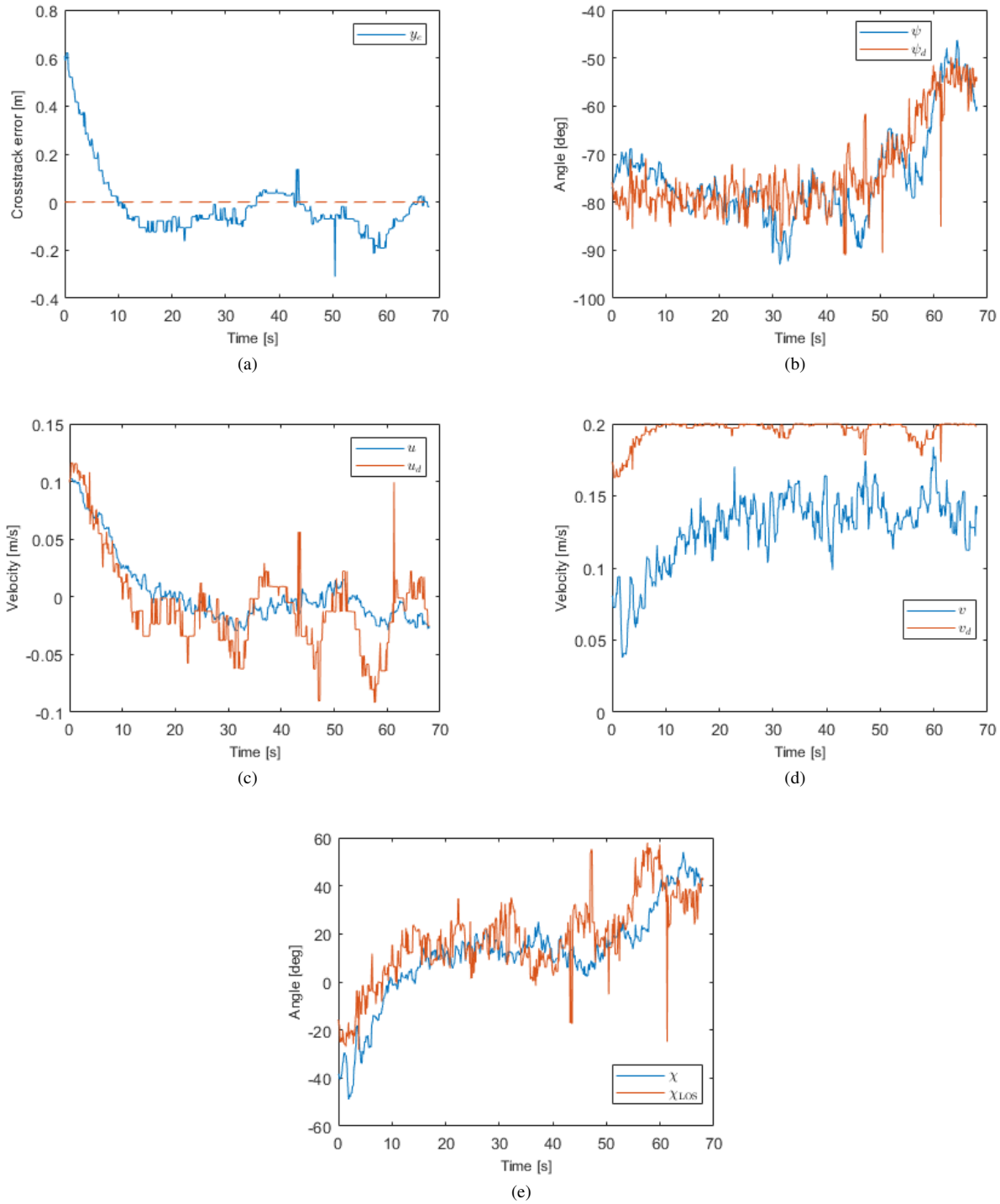

Fig. 17. Experimental results from net pen following trial 2 at SINTEF ACE Rataren. (a) The crosstrack error y_e. (b) The yaw tracking. (c) The surge velocity tracking. (d) The sway velocity tracking. (e) The course angle tracking.

$$\boldsymbol{\phi}_r(u,v,\psi) = \frac{m_{11}^A - m_{22}^A}{m_{33}} \begin{bmatrix} u\sin\psi - v\cos\psi \\ -u\cos\psi - v\sin\psi \\ -\cos\psi\sin\psi \\ \cos\psi\sin\psi \\ 1 - 2\sin^2\psi \end{bmatrix} \tag{49}$$

APPENDIX B
SIMULATION MODEL STATE MATRICES

$$\boldsymbol{M}_{RB} = \begin{bmatrix} 90 & 0 & 0 \\ 0 & 90 & 0 \\ 0 & 0 & 13 \end{bmatrix} \tag{50}$$

$$\boldsymbol{M}_A = \begin{bmatrix} 54 & 0 & 0 \\ 0 & 72 & 0 \\ 0 & 0 & 5.2 \end{bmatrix} \tag{51}$$

$$\boldsymbol{D} = \begin{bmatrix} 250 & 0 & 0 \\ 0 & 200 & 0 \\ 0 & 0 & 15 \end{bmatrix} \tag{52}$$

The thruster allocation matrix $\boldsymbol{B}$ is given by

$$\boldsymbol{B} = \begin{bmatrix} b_{11} & b_{12} & b_{13} & b_{14} \\ b_{21} & b_{22} & b_{23} & b_{24} \\ b_{31} & b_{32} & b_{33} & b_{34} \end{bmatrix} \tag{53}$$

where the elements can be calculated from

$$\begin{aligned} b_{1i} &= \cos\alpha_i \\ b_{2i} &= \sin\alpha_i \\ b_{3i} &= l_{x_i}\sin\alpha_i - l_{y_i}\cos\alpha_i \end{aligned} \tag{54}$$

with $i \in \{1,2,3,4\}$ and $\alpha_i, l_{x_i}, l_{y_i}$ given in Table I.

TABLE I
THRUSTER CONFIGURATION PARAMETERS

Azimuth angles:	$\alpha_1 = 35^\circ$	$\alpha_2 = -35^\circ$
	$\alpha_3 = 35^\circ$	$\alpha_4 = -35^\circ$
Surge position relative to the CO:	$l_{x_1} = 0.202m$	$l_{x_2} = 0.202m$
	$l_{x_3} = -0.265m$	$l_{x_4} = -0.265m$
Sway position relative to the CO:	$l_{y_1} = -0.216m$	$l_{y_2} = 0.216m$
	$l_{y_3} = 0.195m$	$l_{y_4} = -0.195m$

ACKNOWLEDGMENT

The results shown in this paper are part of the Artifex project (pr. number 256241) funded by The Research Council of Norway (RCN). The authors would like to thank the project owner Maritime Robotics AS as well as the project partners Argus Remote Systems AS and Lerow AS for providing assistance during the ROV operations. The work was also supported by activities from: SINTEF ACE, SFI Exposed and the RCN project 269087 (CageReporter). In particular, the authors would like to thank Water Linked AS, the project owner of CageReporter, for borrowing their underwater positioning equipment for validation purposes. The work was also partly supported by the Research Council of Norway through the Centres of Excellence funding scheme, project No. 223254 – NTNU AMOS.

REFERENCES

[1] FAO, *The State of World Fisheries and Aquaculture 2018 – meeting the sustainable development goals*, 2018, accessed on 25 March 2020. [Online]. Available: http://www.fao.org/fishery/sofia/en

[2] Østen Jensen, T. Dempster, E. Thorstad, I. Uglem, and A. Fredheim, "Escapes of fish from Norwegian sea-cage aquaculture: causes, consequences, and prevention," *Aquaculture Environment Interactions*, vol. 1, pp. 71–83, Aug. 2010.

[3] J. Bannister, M. Sievers, F. Bush, and N. Bloecher, "Biofouling in marine aquaculture: a review of recent research and developments," *Biofouling*, vol. 35, no. 6, pp. 631–648, 2019.

[4] M. Føre, K. Frank, T. Norton, E. Svendsen, J. A. Alfredsen, T. Dempster, H. Eguiraun, W. Watson, A. Stahl, L. M. Sunde, C. Schellewald, K. R. Skøien, M. O. Alver, and D. Berckmans, "Precision fish farming: A new framework to improve production in aquaculture," *Biosystems Engineering*, vol. 173, pp. 176 – 193, 2018.

[5] M. Yang, Z. Sheng, Y. Che, J. Hu, K. Hu, and Y. Du, "Design of small monitoring ROV for aquaculture," in *Proc. OCEANS 2019 - Marseille*, 2019, pp. 1–9.

[6] G. Li, Y. Deng, O. L. Osen, S. Bi, and H. Zhang, "A bio-inspired swimming robot for marine aquaculture applications: From concept-design to simulation," in *Proc. OCEANS 2016 - Shanghai*, 2016, pp. 1–7.

[7] Y. Wang, R. Wang, S. Wang, M. Tan, and J. Yu, "Underwater bioinspired propulsion: From inspection to manipulation," *IEEE Transactions on Industrial Electronics*, vol. 67, no. 9, pp. 7629–7638, 2020.

[8] J. Sverdrup-Thygeson, E. Kelasidi, K. Y. Pettersen, and J. T. Gravdahl, "The underwater swimming manipulator—a bioinspired solution for subsea operations," *IEEE Journal of Oceanic Engineering*, vol. 43, no. 2, pp. 402–417, 2018.

[9] P. Lader, D. Kristiansen, M. Alver, H. V. Bjelland, and D. Myrhaug, "Classification of Aquaculture Locations in Norway With Respect to Wind Wave Exposure," in *Proc. ASME 2017 36th International Conference on Ocean, Offshore and Arctic Engineering*, vol. 6: Ocean Space Utilization, Jun. 2017.

[10] D. Kristiansen, V. Aksnes, B. Su, P. Lader, and H. V. Bjelland, "Environmental Description in the Design of Fish Farms at Exposed Locations," in *Proc. ASME 2017 36th International Conference on Ocean, Offshore and Arctic Engineering*, vol. 6: Ocean Space Utilization, Jun. 2017.

[11] P. Lader, T. Dempster, A. Fredheim, and Østen Jensen, "Current induced net defomrations in full-scale sea-cages for Atlantic salmon (Salmo salar)," *Aquaculture Engineering*, vol. 38, pp. 52–65, 2008.

[12] P. Klebert, Øystein Patursson, P. C. Endresen, P. Rundtop, J. Birkevold, and H. W. Rasmussen, "Three-dimensional deformation of a large circular flexible sea cage in high currents: Field experiment and modeling," *Ocean Engineering*, vol. 104, pp. 511 – 520, 2015.

[13] V. Chalkiadakis, N. Papandroulakis, G. Livanos, K. Moirogiorgou, G. Giakos, and M. Zervakis, "Designing a small-sized autonomous underwater vehicle architecture for regular periodic fish-cage net inspection," in *Proc. 2017 IEEE International Conference on Imaging Systems and Techniques (IST)*, Oct 2017.

[14] G. Livanos, M. Zervakis, V. Chalkiadakis, K. Moirogiorgou, G. Giakos, and N. Papandroulakis, "Intelligent navigation and control of a prototype autonomous underwater vehicle for automated inspection of aquaculture net pen cages," in *Proc. 2018 IEEE International Conference on Imaging Systems and Techniques (IST)*, Oct 2018.

[15] F. Dukan and A. J. Sørensen, "Sea Floor Geometry Approximation and Altitude Control of ROVs," *Control Engineering Practice*, vol. 29, pp. 135–146, Aug. 2014.

[16] M. Caccia, R. Bono, G. Bruzzone, and G. Veruggio, "Bottom-following for remotely operated vehicles," *Control Engineering Practice*, no. 11, pp. 461–470, 2003.

[17] P. Rundtop and K. Frank, "Experimental evaluation of hydroacoustic instruments for ROV navigation along aquaculture net pens," *Aquaculture Engineering*, vol. 74, pp. 143–156, Sep. 2016.

[18] K. Y. Pettersen and E. Lefeber, "Way-point tracking control of ships," in *Proc. 40th IEEE Conference on Decision and Control*, Dec. 2001, pp. 940–945.

[19] T. I. Fossen, M. Breivik, and R. Skjetne, "Line-of-sight path following of underactuated marine craft," in *Proc. 6th IFAC Conference on Manoeuvring and Control of Marine Craft (MCMC 2003)*, Sep. 2003.

[20] E. Borhaug, A. Pavlov, and K. Y. Pettersen, "Integral LOS control for path following of underactuated marine surface vessels in the presence of constant ocean currents," in *Proc. 47th IEEE Conference on Decision and Control*, Dec. 2008, pp. 4984–4991.

[21] T. I. Fossen and K. Y. Pettersen, "On uniform semiglobal exponential stability (USGES) of proportional line-of-sight guidance laws," *Automatica*, vol. 50, pp. 2912–2917, 2014.

[22] S. Moe, K. Y. Pettersen, T. I. Fossen, and J. T. Gravdahl, "Line-of-sight curved path following for underactuated USVs and AUVs in the horizontal plane under the influence of ocean currents," in *Proc. 24th Mediterranean Conference on Control and Automation (MED)*, Jun. 2016, pp. 38–45.

[23] W. Caharija, K. Y. Pettersen, M. Bibuli, P. Calado, E. Zereik, J. Braga, J. T. Gravdahl, A. J. Sørensen, M. Milovanović, and G. Bruzzone, "Integral line-of-sight guidance and control of underactuated marine vehicles: Theory, simulations, and experiments," *IEEE Transactions on Control Systems Technology*, vol. 24, no. 5, pp. 1623–1642, Sep. 2016.

[24] W. Caharija, K. Y. Pettersen, and J. T. Gravdahl, "Path following of marine surface vessels with saturated transverse actuators," in *Proc. American Control Conference*, Jun. 2013, pp. 546–553.

[25] F. Dukan, "ROV motion control systems," Ph.D. dissertation, Norwegian University of Science and Technology, 2014.

[26] M. Breivik and T. I. Fossen, "Guidance-based path following for autonomous underwater vehicles," in *Proc. OCEANS 2005 MTS/IEEE*, Sep. 2005, pp. 2807 – 2814 Vol. 3.

[27] G. Antonelli, *Underwater Robots*. Springer, 2018.

[28] S. Martin and L. Whitcomb, "Experimental identification of three degree-of-freedom coupled dynamic plant models for underwater vehicles," in *Sensing and Control for Autonomous Vehicles: Applications to Land, Water and Air Vehicles*, T. I. Fossen, K. Y. Pettersen, and H. Nijmeijer, Eds. Springer, 2017.

[29] T. I. Fossen, *Handbook of Marine Craft Hydrodynamics and Motion Control*. John Wiley & Sons, Ltd., 2011.

[30] C. H. Edwards and D. E. Penney, *Elementary linear algebra*. Prentice Hall, 1988.

[31] I.-L. G. Borlaug, K. Y. Pettersen, and J. T. Gravdahl, "Trajectory tracking for an articulated intervention AUV using a super-twisting algorithm in 6DOF," in *Proc. 11th IFAC Conference on Control Applications in Marine Systems, Robotics, and Vehicles*, Sep. 2018, pp. 311–316.

[32] I.-L. Borlaug, J. Sverdrup-Thygeson, K. Pettersen, and J. Gravdahl, "Combined kinematic and dynamic control of an underwater swimming manipulator," *Mechatronics*, vol. 69, 2020.

[33] L. Qiao and W. Zhang, "Double-loop integral terminal sliding mode tracking control for UUVs with adaptive dynamic compensation of uncertainties and disturbances," *IEEE Journal of Oceanic Engineering*, vol. 44, no. 1, pp. 29–53, 2019.

[34] L. Qiao and W. Zhang, "Adaptive non-singular integral terminal sliding mode tracking control for autonomous underwater vehicles," *IET Control Theory Applications*, vol. 11, no. 8, pp. 1293–1306, 2017.

[35] T. I. Fossen and S. I. Sagatun, "Adaptive control of nonlinear underwater robotic systems," *Modeling, Identification and Control*, vol. 12, no. 2, pp. 95–105, 1991.

[36] G. Antonelli, S. Chiaverini, N. Sarkar, and M. West, "Adaptive control of an autonomous underwater vehicle: experimental results on ODIN," *IEEE Transactions on Control Systems Technology*, vol. 9, no. 5, pp. 756–765, 2001.

[37] H. K. Khalil, *Nonlinear Systems*. Prentice Hall, Inc., 2002.

[38] P. Ioannou and J. Sun, *Robust Adaptive Control*. Dover Publications, 1996.

[39] E. D. Sontag, "A remark on the converging-input converging-state property," *IEEE Transactions on Automatic Control*, vol. 48, no. 2, pp. 313–314, Feb. 2003.

[40] K.-J. Reite, M. Føre, K. G. Aarsæther, J. Jensen, P. Rundtop, L. T. Kyllingstad, P. C. Endresen, D. Kristiansen, V. Johansen, and A. Fredheim, "Fhsim - time domain simulations of marine systems," in *Proc. ASME 2014 33rd International Conference on Ocean, Offshore and Arctic Engineering*, Jun. 2014.

[41] B. Su, K.-J. Reite, M. Føre, K. G. Aarsæther, M. Alver, P. C. Endresen, D. Kristiansen, J. Haugen, W. Caharija, and A. Tsarau, "A multipurpose framework for modelling and simulation of marine aquaculture systems," in *Proc. ASME 2019 38th International Conference on Ocean, Offshore and Arctic Engineering*, Dec. 2019.

[42] M. Føre, J. Alfredsen, V. Johansen, and D. Johansson, "Modelling of Atlantic salmon (Salmo salar L.) behaviour in sea-cages: A Lagrangian approach," *Aquaculture*, vol. 288, no. 3-4, pp. 196 – 204, March 2009.

[43] M. Føre, T. Dempster, J. A. Alfredsen, and F. Oppedal, "Modelling of Atlantic salmon (Salmo salar L.) behaviour in sea-cages: Using artificial light to control swimming depth," *Aquaculture*, vol. 388-391, pp. 137 – 146, 2013.

[44] M. Føre, M. Alver, J. A. Alfredsen, G. Marafioti, G. Senneset, J. Birkevold, F. V. Willumsen, G. Lange, Åsa Espmark, and B. F. Terjesen, "Modelling growth performance and feeding behaviour of Atlantic salmon (Salmo salar L.) in commercial-size aquaculture net pens: Model details and validation through full-scale experiments," *Aquaculture*, vol. 464, pp. 268 – 278, 2016.

[45] D. Johansson, F. Laursen, A. Fernö, J. Fosseidengen, P. Klebert, L. Stien, T. Vågseth, and F. Oppedal, "The interaction between water currents and salmon swimming behaviour in sea cages," *PloS one*, vol. 9, May 2014.

Herman B. Amundsen received the MSc degree in cybernetics and robotics from the Norwegian University of Science and Technology (NTNU), Trondheim, Norway, in 2020.

He is with SINTEF Ocean AS, Trondheim, Norway, where he has been employed since 2019 and the Department of Engineering Cybernetics, NTNU where he is a PhD student since 2021. His research interests include guidance and control of marine vehicles, underwater robotics and autonomy in aquaculture.

Walter Caharija received a MSc in electrical engineering from the University of Trieste, Italy, in 2009 and obtained a PhD in engineering cybernetics from the Norwegian University of Science and Technology, Norway, in 2014. During his PhD he worked in the field of marine control, focusing on guidance systems as well as control techniques capable of handling and compensating sea loads such as wind, waves and currents.

From 2014 until 2017 he was employed at the Lloyd's Register in Norway where he was involved in software assurance, analysis of dynamic positioning systems, RAMS, collision avoidance systems and autonomous vehicles. Since 2017 he has been employed by SINTEF Ocean as a research scientist where he is involved in the following activities: underwater robotics, automation and instrumentation for aquaculture, product development as well as modeling of physical and biological systems. Walter has co-authored over 20 peer-reviewed conference and journal papers, was awarded of the 2017 IEEE Transactions on Control Systems Technology Outstanding Paper Award and he was the recipient of the 2017 SINTEF's Award for Excellence in Research.

Kristin Y. Pettersen (M'92-SM'04-F'17) received the MSc and PhD degrees in engineering cybernetics from the Norwegian University of Science and Technology (NTNU), Trondheim, Norway, in 1992 and 1996, respectively. She is a Professor in the Department of Engineering Cybernetics, NTNU, where she has been a faculty member since 1996. She was Head of Department 2011-2013, Vice-Head of Department 2009-2011, and Director of the NTNU ICT Program of Robotics 2010-2013. She is Adjunct Professor at the Norwegian Defence Research Establishment (FFI). In the period 2013 – 2022 she is also Key Scientist at the CoE Centre for Autonomous Marine Operations and Systems. She is a co-founder of the NTNU spin-off company Eelume AS, where she was CEO 2015-2016.

She has published four books and more than 250 papers in international journals and conference proceedings. Her research interests focus on nonlinear control of mechanical systems with applications to robotics, with a special emphasis on marine robotics and snake robotics. She was awarded the IEEE Transactions on Control Systems Technology Outstanding Paper Award in 2006 and in 2017, and received the IEEE CSS 2020 Hendrik W. Bode Lecture Prize.

She was a member of the IEEE Control Systems Society Board of Governors 2012 – 2014 and is currently a member of the IFAC Council and the EUCA Council. She has also held and holds several board positions in industrial and research companies. She has served as Associate Editor of IEEE Transactions on Control Systems Technology and IEEE Control Systems Magazine, and is currently Senior Editor of IEEE Transactions on Control Systems Technology. She is IEEE CSS Distinguished Lecturer 2019-2021, IEEE Fellow, member of the Norwegian Academy of Technological Sciences, and member of the Academy of the Royal Norwegian Society of Sciences and Letters.